Gross Moist Stability and MJO Simulation Skill in Three Full-Physics GCMs

JAMES J. BENEDICT* AND ERIC D. MALONEY
Department of Atmospheric Science, Colorado State University, Fort Collins, Colorado

ADAM H. SOBEL
Department of Applied Mathematics, and Department of Earth and Environmental Sciences, and Lamont-Doherty Earth Observatory, Columbia University, New York, New York

DARGAN M. W. FRIERSON
Department of Atmospheric Sciences, University of Washington, Seattle, Washington

(Manuscript received 5 August 2013, in final form 14 May 2014)

ABSTRACT

Previous studies have demonstrated a link between gross moist stability (GMS) and intraseasonal variability in theoretical and reduced-complexity models. In such simplified models, MJO-like moisture modes—convectively coupled tropical disturbances akin to the MJO whose formation and dynamics are linked to moisture perturbations—develop only when GMS is either negative or ''effectively'' negative when considering additional sources of moist entropy. These simplified models typically use a prescribed, time-independent GMS value. Limited work has been done to assess GMS and its connection to intraseasonal variability in full-physics general circulation models (GCMs).

The time-mean and intraseasonal behavior of normalized GMS (NGMS) are examined in three pairs of GCMs to elucidate the possible importance of NGMS for the MJO. In each GCM pair, one member produces weak intraseasonal variability, while the other produces robust MJOs because of a change in the treatment of deep convection. A strong linear correlation between time-mean NGMS and MJO simulation skill is observed, such that GCMs with less positive NGMS produce improved MJO eastward propagation. The reduction in time-mean NGMS is primarily due to a sharp drop to negative values in the NGMS component related to vertical advection, while the horizontal advection component has a less clear relationship with MJO simulations. Intraseasonal fluctuations of anomalous NGMS modulate the magnitude of background NGMS but generally do not change the sign of background NGMS. NGMS declines ahead of peak MJO rainfall and increases during and after heaviest precipitation. Total NGMS fluctuates during MJO passage but remains positive, suggesting that other sources of moist entropy are required to generate an effectively negative NGMS.

1. Introduction

The interaction between cumulus convection and the large-scale flow in which it is embedded is a hallmark feature of many tropical weather systems, including the Madden–Julian oscillation (MJO) (Madden and Julian 1971; Zhang 2005). Despite decades of advancement of conceptual theories, enhanced modeling capabilities, and a greater scope and quality of tropical atmospheric measurements, our understanding of such interactions remains incomplete. One approach to examining the relationship between convective cloud systems and large-scale dynamics utilizes the concept of gross moist stability (GMS) (Neelin and Held 1987). GMS quantifies the moist static energy or moist entropy export in a convective overturning circulation per unit of mass transport. GMS also emerges naturally as a key parameter in reduced-complexity models for tropical dynamics. In this study, we examine GMS in several pairs of general circulation models (GCMs) as a means of

---

* Current affiliation: Lawrence Berkeley National Laboratory, Berkeley, California.

Corresponding author address: James J. Benedict, Lawrence Berkeley National Laboratory, 1 Cyclotron Rd., MS 74-0171, Berkeley, CA 94720.
E-mail: jjbenedict@lbl.gov

DOI: 10.1175/JAS-D-13-0240.1

diagnosing the role that GMS might play in determining the GCM's ability to realistically simulate the MJO.

No single conceptual theory has yet been able to provide a comprehensive picture of the key elements of MJO behavior. Leading theories highlight tropical instabilities arising from a number of mechanisms, including local thermodynamic processes (Bladé and Hartmann 1993; Bony and Emanuel 2005), surface turbulent fluxes (Emanuel 1987; Sobel et al. 2010), and wave–convection interactions that include a frictional boundary layer (Wang 1988; Wang and Rui 1990). Of relevance to the present study, a number of studies interpret the MJO as a moisture mode (Sobel et al. 2001; Fuchs and Raymond 2005; Raymond and Fuchs 2009; Sobel and Maloney 2012) or large-scale convectively coupled disturbance whose properties are controlled primarily by mechanisms that govern the evolution of the moisture field and that would not exist in a mathematical model that lacks a prognostic moisture equation.

One approach to testing conceptual theories as a means of understanding how tropical convection interacts with its environment is through the use of simplified models. A diverse spectrum of theoretical models has been developed to examine relationships among convection, moisture distribution, radiation, and surface fluxes (e.g., Emanuel et al. 1994; Neelin and Yu 1994; Neelin and Zeng 2000; Fuchs and Raymond 2002, 2005; Raymond and Fuchs 2007, 2009; Sugiyama 2009). Many theoretical studies focusing on such interactions have implemented the weak temperature gradient (WTG) approximation, which is a simplified dynamical framework that takes advantage of the spatial uniformity of temperature in the tropics (e.g., Charney 1963; Held and Hoskins 1985; Sobel et al. 2001). Organized convective disturbances whose development and dynamics are closely linked to moisture perturbations—so-called moisture modes—become unstable in such models either when GMS is negative or when "effective" GMS, including radiative or surface flux feedbacks (Su and Neelin 2002; Bretherton and Sobel 2002; Sugiyama 2009; Sobel and Maloney 2012, 2013), is negative.

In order for the GMS to be part of a successful theory for tropical precipitation, we ultimately need a theory for the value of GMS itself as a function of environmental conditions. The observational study of López Carrillo and Raymond (2005) indicates that GMS is a function of saturation fraction, where relatively drier regimes have lower column moisture and import s (GMS < 0) while regimes with higher column moisture export s (GMS > 0). Consistent with this, single-column models (SCMs) and cloud-resolving models (CRMs) run in WTG mode can produce two stable equilibria for the same boundary conditions and forcings. One corresponds to dry conditions and has GMS < 0; this still implies export of moist static energy but associated with a descending large-scale circulation. The other corresponds to wet conditions and has GMS > 0 (Sobel et al. 2007; Sessions et al. 2010). These SCM and CRM results are consistent with those of Bretherton et al. (2005), who noted self-aggregating convective clusters produced in an idealized CRM in radiative–convective equilibrium (RCE) on a large domain. The clusters and dry regimes within the large domain are thought to correspond to the wet and dry regimes in the smaller-domain simulations under WTG (although the correspondence cannot be exact because, in RCE, the dry and wet regimes cannot both export moist static energy, as they can in the WTG solutions, because the net export of moist static energy from a domain in RCE must vanish). Though simplistic, these results form the foundation of our view of the cyclic convectively suppressed and active phases observed in large-scale tropical disturbances such as the MJO.

Observational and modeling evidence supports the utility of GMS as a diagnostic relevant to the dynamics of tropical convective disturbances. Satellite measurements of the tropical atmosphere indicate that the initiation and distribution of deep convective precipitation is a sharply increasing function of the amount of moisture in the ambient lower and middle troposphere (Sherwood 1999; Bretherton et al. 2004; Holloway and Neelin 2009). Assuming WTG conditions, perturbations of column-integrated moisture are nearly equivalent to perturbations of column-integrated moist entropy. By linking convective intensity with atmospheric processes that regulate column moist entropy, GMS represents a valuable parameter that can be used to diagnose organized tropical precipitation. For example, Frierson et al. (2011), Hannah and Maloney (2011), Pritchard and Bretherton (2014), and Hannah and Maloney (2014) have highlighted relationships between GMS and intraseasonal convective disturbances in individual GCMs with modified treatments of deep convection. Regardless, a more thorough understanding is needed of the potential applicability of GMS as a diagnostic of the MJO.

In this study, we analyze the behavior of GMS in three pairs of full-physics GCMs to explore possible systematic relationships between GMS and simulated intraseasonal (20–100 day) variability. We focus on intraseasonal convective disturbances that occur during boreal winter (October–April) when the MJO is most active and marked by dominant eastward propagation (Salby and Hendon 1994). In each pair of GCMs, one member produces weak intraseasonal variability

TABLE 1. Highlighted features of the GCMs examined in this study. Here, L represents the number of GCM levels, RAS is the Relaxed Arakawa–Schubert scheme of Moorthi and Suarez (1992), ZM95 is the Zhang–McFarlane (Zhang and McFarlane 1995) scheme, α is the Tokioka et al. (1988) parameter, and ISV qualitatively describes intraseasonal variability within the simulation. SPCAM-AMIP is the superparameterized version of CAM3 forced with prescribed sea surface temperatures in the style of the Atmosphere Model Intercomparison Project (AMIP). See text for further details.

		Deep convection parameterization				
Simulation	GCM resolution	Scheme	Closure	Trigger	Downdrafts?	ISV
AM2-CTL	2° lat × 2.5° lon, L24	RAS	CAPE relaxation	$\alpha = 0.025$	No	Weak
AM2-TOK	2° lat × 2.5° lon, L24	RAS	CAPE relaxation	$\alpha = 0.1$	No	Strong
AM3-CTL	~163–231 km, L32	Donner	CAPE relaxation	—	No	Weak
AM3-A	~163–231 km, L32	Donner	Zhang (2002) (CAPE based)	Time-integrated low-level parcel lifting	Yes	Strong
CAM3	T42 (~2.8° × 2.8°), L30	ZM95	CAPE consumed at specified rate	—	Yes	Weak
SPCAM-AMIP	T42 (~2.8° × 2.8°), L30	Explicit (4-km CRM)	—	—	Explicit	Strong

while its counterpart produces stronger intraseasonal variability and more realistic MJO disturbances owing to a change in the treatment of deep convection. Our goal is to investigate what role, if any, GMS plays in explaining the differences seen within each GCM pair. Our analysis will examine both the time-mean GMS and its intraseasonal fluctuations. Hannah and Maloney (2011) analyzed a series of GCM simulations in a single model and found a reduction in time-mean GMS when minimum cumulus entrainment and rain evaporation were increased to produce stronger MJO activity. Intraseasonal variability in GMS was also increased with such modifications. Additionally, Frierson et al. (2011) ascribed the slower propagation of convectively coupled Kelvin waves in a suite of GCM simulations with modified convective parameterizations to reduced time-mean GMS. As suggested by Raymond et al. (2009), the assessment of GMS in simulations with different cumulus parameterization schemes may help us understand model weaknesses by highlighting processes that are unrealistically suppressed or overemphasized.

A description of the data sources and a review of the model simulations are presented in section 2. We provide a commentary on the calculation and utility of GMS in section 3. Our primary findings are presented in section 4, followed by a discussion of the results and concluding remarks in section 5.

2. Data and model description

We investigate the behavior of GMS and related variables in three pairs of GCMs, resulting in a total of six simulations. In each GCM pair, one model version produces weak tropical intraseasonal variability (the "control" simulation) while the other member produces stronger intraseasonal variability owing to a modification in the treatment of deep convection (the "modified" simulation). Table 1 lists the GCM simulations examined in this study and other salient information related to their treatments of deep convection.

The first GCM pair consists of two versions of the Geophysical Fluid Dynamics Laboratory (GFDL) Atmosphere Model version 2 (AM2) (Anderson et al. 2004). Both versions of the AM2 parameterize cumulus convection using the relaxed Arakawa–Schubert (RAS) (Moorthi and Suarez 1992) scheme consisting of a spectrum of entraining plumes. Also included is a modification that suppresses deep convective updrafts with lateral entrainment rates below a minimum threshold $\mu_{\min} = \alpha/D$, where α is a positive constant and D is the subcloud-layer depth (Tokioka et al. 1988). Consistent with previous studies (Hannah and Maloney 2011; Kim et al. 2011; Hannah and Maloney 2014), increasing the value of α in AM2-TOK results in stronger intraseasonal variability (see section 4).

The second GCM pair consists of two versions of the GFDL AM3 (Donner et al. 2011). Many features of AM3 differ greatly from those of AM2, including the dynamical core, spatial grid, and treatment of deep and shallow convection [see Donner et al. (2011) or Benedict et al. (2013) for further details]. The deep convection scheme includes parameterizations for both deep cumulus plumes and, unlike in AM2, dynamically active mesoscale anvil clouds that modulate local radiative fluxes and water substance transport between the cumuli and their environment. In AM3-CTL, the convective closure assumption is based on relaxing CAPE back to a reference value over a specified time scale, and convective downdrafts are not parameterized. In the modified AM3 (AM3-A), the default CAPE relaxation closure is replaced by the Zhang (2002) closure. A convective trigger that requires time-integrated low-level parcel ascent to exceed a specified magnitude for deep cumuli to form (Donner et al. 2001) is also added.

Although neglected in AM3-CTL, convective downdrafts are parameterized in AM3-A, so we expect stronger interactions between convection and environmental moisture. The modifications to the treatment of deep convection in the AM3 result in stronger intraseasonal variability at the expense of a degraded mean state (see Fig. 1).

The final GCM pair consists of version 3.0 of the standard National Center for Atmospheric Research (NCAR) Community Atmosphere Model (CAM) (Collins et al. 2006) and its superparameterized (SP) variant, the SPCAM (Khairoutdinov et al. 2008, hereafter KDR08). Both simulations are run using a semi-Lagrangian dynamical core at 2.8° × 2.8° horizontal resolution (T42 spectral truncation). The Zhang–McFarlane (Zhang and McFarlane 1995) deep convection scheme employed by CAM3.0 accounts for convective downdrafts and assumes that CAPE is consumed by cumuli at a specified rate. CAM3 acts as the host GCM for the SPCAM simulation. Using the SP approach, a 2D north–south-oriented ‘‘curtain’’ CRM with 32 columns, 28 levels collocated with the lowest 28 CAM levels, and 4-km horizontal resolution is embedded into each CAM grid cell. The embedded CRMs replace the CAM conventional parameterizations of convection and boundary layer processes. Additional information on the SPCAM simulation examined in this study and the SP approach can be found in KDR08 and Benedict and Randall (2009). Compared to the standard CAM3, notably stronger intraseasonal variability is observed in CAM simulations that utilize the SP approach (KDR08; Benedict and Randall 2009).

All AM simulations are run for 11 years, with the first year discarded to mitigate the effects of model spinup. Lower boundary forcing consists of the climatological (1981 to ~2000) mean seasonal cycle at monthly temporal resolution of SSTs and sea ice concentrations taken from Reynolds et al. (2002) for AM2 and Hurrell et al. (2008) for AM3. The CAM/SPCAM simulations span 19 years (1985–2004) and use observed monthly SSTs and sea ice concentrations (Hurrell et al. 2008), but only data between 1986 and 2003 is presented in this study.

The six GCM simulations are compared to satellite-based precipitation estimates and reanalysis data products. For simple climatological comparison (Fig. 1 only), the simulations are validated against 1980–2000 mean rainfall from the Global Precipitation Climatology Project (GPCP) (Adler et al. 2003) and mean 850-hPa zonal winds from the Interim European Centre for Medium Range Weather Forecasts Re-Analysis (ERA-Interim) (Berrisford et al. 2009). For all other figures, precipitation from the Tropical Rainfall Measuring

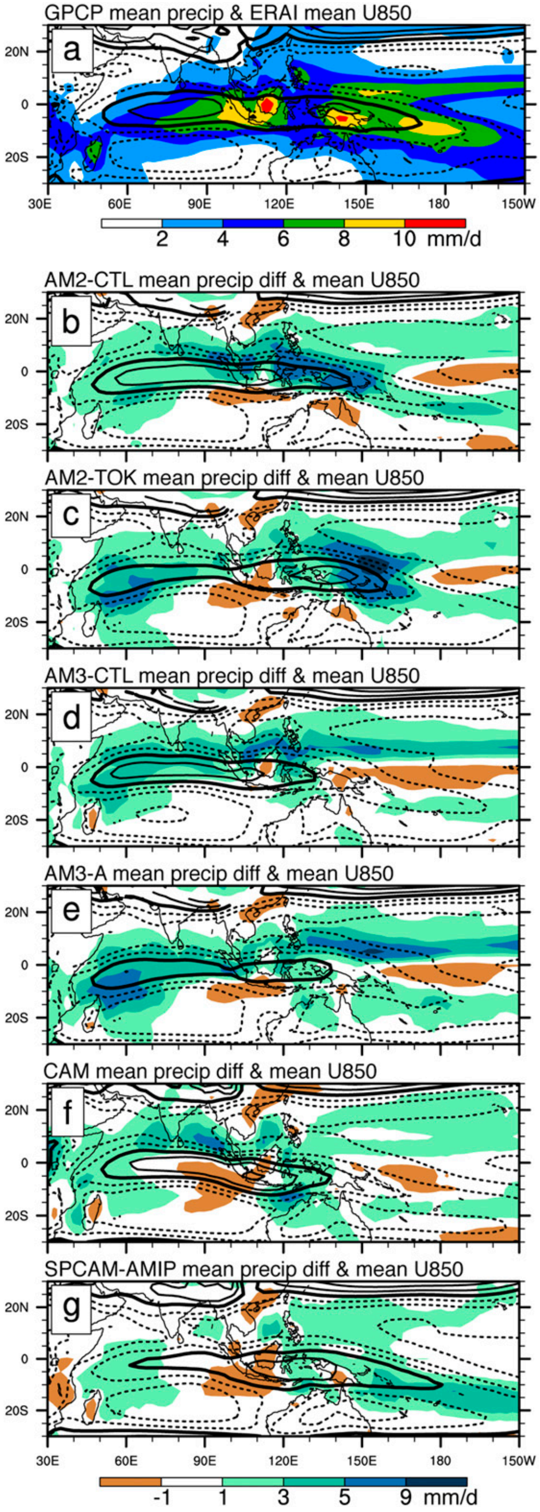

FIG. 1. (a) Boreal winter-mean GPCP precipitation (shaded) and ERA-Interim U_{850} (contours). Wind contours are 0, ±2, ±4, ±8, and $\pm 12\,\mathrm{m\,s^{-1}}$, and positive, zero, and negative contours are thin solid, thick solid, and dashed lines, respectively. (b)–(g) Boreal winter-mean precipitation differences between each model and GPCP (shaded) and mean U_{850} using identical contours as in (a).

Mission (TRMM) 3B42 version 6 data product (Huffman et al. 2007) and dynamic and thermodynamic variables from ERA-Interim during the 1999–2008 period are used to validate the simulations.[1] Differences between the TRMM 3B42 and GPCP rainfall products are insignificant for our purposes (Kim et al. 2014a). Although mostly offset from the simulation time spans, we chose to use the 1999–2008 validation period because satellite-based estimates of precipitation at daily resolution are only available after late 1997. In this paper we will refer to the validation datasets as ''observations,'' but some amount of caution is advised. Few ''ground truth'' meteorological stations exist over the open Indian and west Pacific Ocean regions where the MJO is most active, limiting the rain gauge data that is streamed into the TRMM 3B42 product and forcing ERA-Interim to be more strongly constrained by model parameterizations (rather than radiosondes) in these areas. All model and validation data are daily averaged and linearly interpolated to the 27 ERA-Interim standard pressure levels and a 2.5° horizontal grid. Additionally, we define ''anomaly'' as the departure from a smoothed seasonal cycle.

3. Comments on gross moist stability

Gross moist stability is broadly defined as the ratio of vertically integrated horizontal divergence of an intensive quantity conserved under moist adiabatic processes to some measure of convective intensity. In this study we use specific moist entropy s as the conserved quantity following Raymond et al. (2009) and references therein. GMS thus provides a measure of the efficiency with which convection and associated large-scale circulations discharge s from the column, which in turn allows one to infer the strength of the circulation or precipitation response to a given forcing in the column-integrated s budget. GMS emerges naturally in any theory for tropical dynamics that focuses on the budget of s (or moist static energy)—a variable that is approximately conserved in a moist atmosphere.

We use the following equation for s, which is valid for temperatures either above or below freezing (Raymond 2014):

$$\begin{aligned} s = (C_{PD} + r_V C_{PV}) \ln(T/T_R) - R_D \ln(p_D/p_R) \\ - r_V R_V \ln(p_V/e_{SF}) + (L_V r_V/T_R). \end{aligned} \tag{1}$$

In (1), the specific heat, gas constant, and partial pressure of dry air are C_{PD}, R_D, and p_D, respectively; the specific heat, gas constant, and partial pressure of water vapor are C_{PV}, R_V, and p_V, respectively; r_V is the water vapor mixing ratio; T is air temperature; $T_R = 273.1\,\mathrm{K}$; $e_{SF} = 611\,\mathrm{Pa}$; and $L_V(T) \approx 2.5 \times 10^6\,\mathrm{J\,kg^{-1}}$ is the enthalpy of vaporization. Liquid water and ice mixing ratios do not appear in (1) because they were not written to the GFDL AM daily output files. However, we found that liquid and ice only weakly influence s.

''Normalized'' GMS (NGMS) is derived from the budget of vertically integrated s and may be written as

$$\Gamma_T = -\frac{T_R[\nabla \cdot (s\mathbf{v})]}{L[\nabla \cdot (r\mathbf{v})]}, \tag{2}$$

where r is the water vapor mixing ratio, $\mathbf{v}$ the horizontal vector wind, square brackets indicate a mass-weighted vertical integral from the surface to the tropopause, and other variables are as described in (1). Note that we use vertically integrated moisture convergence as the normalization factor in (2), as opposed to the dry static energy export that is used in some other studies (e.g., Wang and Sobel 2011, 2012; Sobel and Maloney 2012, 2013); results are not expected to be particularly sensitive to this choice. Another difference of convention is that the definition of GMS in (2) is based on the total horizontal flux divergence, which includes horizontal advective tendencies, whereas in some studies the GMS refers only to what is called here the ''vertical component'' [see (3)–(5)] with horizontal advection treated as external.

In steady-state conditions, we can formulate an expression demonstrating the sensitivity of net precipitation to NGMS as $P = E + T_R(F_S - R)/L\Gamma_T$. Here, P and E are time-mean precipitation and evaporation, respectively; F_S is the surface entropy flux; and R is the column entropy sink due to radiative cooling. The expression indicates that precipitation, at least in the time mean, becomes a stronger function of entropy forcing $(F_S - R)$ if NGMS is small. The entropy forcing increases when F_S increases owing to larger surface evaporative or sensible heat fluxes or when R decreases owing to reduced longwave cooling to space in the presence of abundant upper-level cloudiness and moisture.

If we do not assume a steady state, but we do assume that free tropospheric temperature variations are small, then the sign of NGMS tells us how convection feeds back onto the moisture field (Raymond 2000). If NGMS is negative, convection strong enough to drive large-scale ascent results in an increase in column moist static energy, thus promoting an environment favorable for future convection. If NGMS is positive, convection and

---

[1] For moist entropy budget plots shown in Fig. 11, surface latent heat fluxes are taken from the objectively analyzed surface flux dataset, as described in Yu and Weller (2007).

large-scale ascent dry the environment despite moisture convergence. As a simple example, we highlight the link between cloud characteristics and the NGMS vertical component [see (5)]: we associate negative NGMS with shallow convective or congestus cloud regimes and a net import of column s, while positive NGMS is characterized by more mature convection and cumulonimbi-driven stratiform clouds that produce a net export of column s. An informative review of GMS can be found in Raymond et al. (2009).

Following Raymond et al. (2007) and Raymond et al. (2009), we can define the total, horizontal, and vertical advective components of the NGMS as

$$\Gamma_T = -\frac{T_R[\mathbf{v}\cdot\nabla s + \omega(\partial s/\partial p)]}{L[\nabla\cdot(r\mathbf{v})]}, \tag{3}$$

$$\Gamma_H = -\frac{T_R[\mathbf{v}\cdot\nabla s]}{L[\nabla\cdot(r\mathbf{v})]}, \tag{4}$$

$$\Gamma_V = -\frac{T_R[\omega(\partial s/\partial p)]}{L[\nabla\cdot(r\mathbf{v})]}. \tag{5}$$

In (3)–(5), $\mathbf{v}$ is the horizontal vector wind, ω is the vertical pressure velocity, p is the atmospheric pressure, ∇ is the gradient operator on a constant-pressure surface, and other notations and variable definitions are as described in (2). We again neglect the presence of liquid and ice. All spatial derivatives are computed before interpolation to a unified 2.5°-resolution and 27-level grid, and, when calculating horizontal derivatives, we account for small horizontal pressure changes along a given level of the model hybrid coordinate. Horizontal advection is calculated in a reference frame fixed to Earth's surface, but this choice is unlikely to significantly impact our horizontal advection values or our overall conclusions, given that MJO-like disturbances generally propagate several times faster than the weak mean zonal flow in the Indo-Pacific region (see Fig. 1). The choice of a horizontally stationary or moving reference frame does not affect vertical advection terms. The classically defined Neelin and Held (1987) form of GMS is most closely related to (5). We elect to use the advective form of Γ_T [(3)] rather than its flux form [(2)]. Arakawa (2004) demonstrates that budget considerations of intensive quantities such as s are best characterized using the advective form rather than the flux form of the advection equation.

To generate a statistically stable quantity, substantial space–time averaging of terms that make up (3)–(5) is required. Following the methods outlined in Raymond et al. (2009), we first average the numerator and denominator separately and then combine them to obtain NGMS. For time-mean plots of NGMS (e.g., Figs. 6 and 7), we apply a 17-day running average and a 7.5° sliding-box smoothing centered at each grid point to numerator and denominator separately. No land points are included in any spatial averaging. For NGMS calculations that do not involve taking climatological means (e.g., Fig. 10), the sliding-box smoothing expands slightly to 12.5°. Of several space–time smoothing approaches tested, this one yielded a satisfying compromise between statistical stability and preservation of MJO-scale features. To avoid division by zero and reduce noise, NGMS values are discarded wherever vertically integrated moisture convergence is less than $|5|\ \mathrm{W\,m^{-2}}$ (for Fig. 10, less than $|30|\ \mathrm{W\,m^{-2}}$). The basic features discussed in section 4 are not sensitive to reasonably small changes in this smoothing approach.

Several issues arise regarding our choice of the total and vertical components of column-integrated s advection and the potential sources of error in our computations of these quantities. First, all advection calculations are made on postprocessed data and not within the model integration itself, which may introduce errors due to space–time interpolation and averaging. For example, large differences between CAM advection terms computed during integration using spherical harmonics and those computed during postprocessing are known to exist. Second, a strong sensitivity to the chosen limits of column integration exists. Deep convective areas typically have a large convergence of s near the surface and slightly larger divergence of s near the tropopause, indicating that vertically integrated advection may be a residual of two large terms. Third, ω is small but not zero at the top and bottom of our chosen atmospheric column (surface and 100 hPa, respectively), while we do assume $\omega = 0$ when formulating the vertical integrals of either the flux or advective forms of s advection. These three issues contribute to nonnegligible differences between the flux and advective forms of Γ_T. Over the Indo-Pacific, the temporal correlations between these two forms range from 0.3 in CAM to >0.9 in AM2 (both values are statistically significant above the 99% level), but the corresponding local rms differences can exceed the local standard deviation, indicating that in some instances the errors may be large compared to typical magnitude fluctuations.

4. Results

a. Basic assessment of time-mean variables and intraseasonal variability

Figure 1a shows October–April (boreal winter)-mean precipitation and 850-hPa zonal winds (U_{850}) based on GPCP and ERA-Interim, respectively, and Figs. 1b–g the boreal winter-mean precipitation

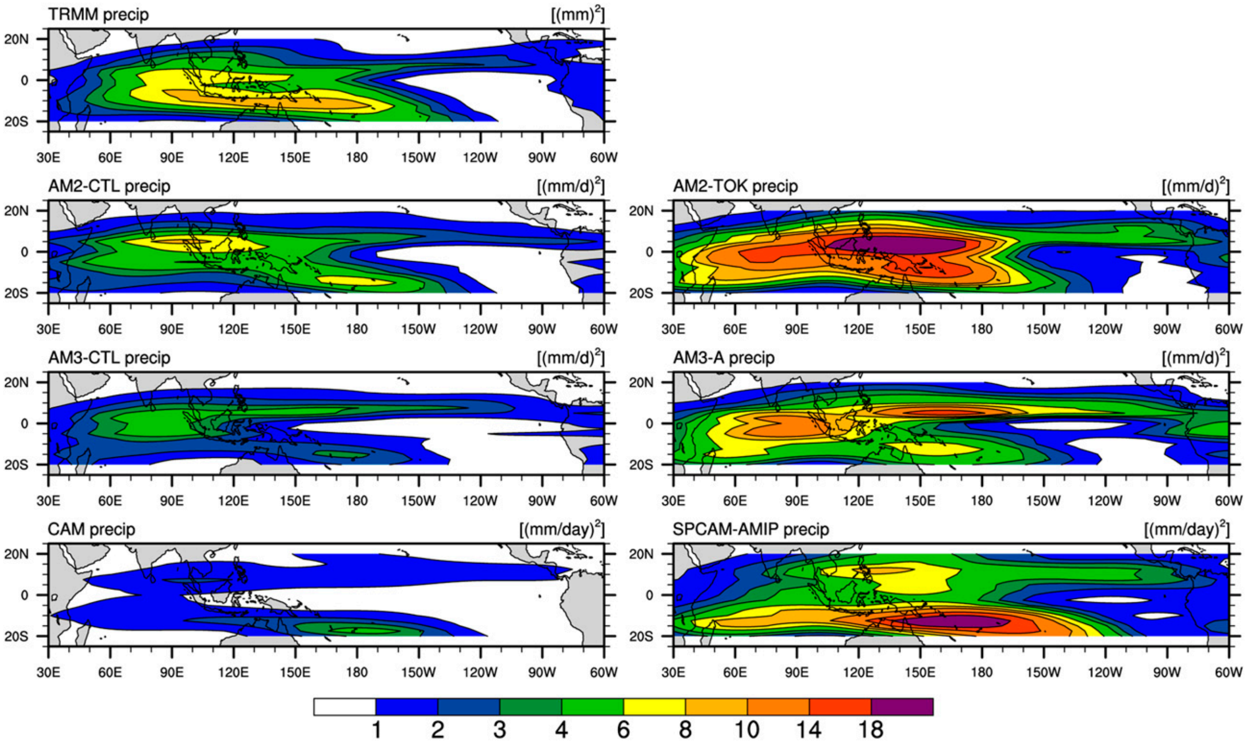

FIG. 2. Boreal winter variance of MJO-filtered precipitation. The filter retains only eastward-propagating disturbances for zonal wavenumbers +1 to +6 and periods 20–100 days.

differences (model - GPCP) and the mean U_{850} for each simulation. Details of the simulation biases are reported in other studies (Benedict and Randall 2007; Benedict et al. 2013), but here we briefly highlight features most relevant to the MJO. Despite very different deep convective parameterizations, the changes seen in U_{850} between the control and modified simulations are surprisingly consistent among the GCM pairs. In each control run, the strip of equatorial U_{850} westerlies in the Indian Ocean is realistic, but its eastward extension is too limited compared to observations. All modified simulations—those producing an improved MJO—display weakened westerlies in the Indian Ocean, while AM2-TOK and SPCAM display a tendency to extend the westerlies farther into the west Pacific, as is seen in reanalysis. Each simulation generally overestimates Indo-Pacific rainfall, particularly in the west and northeast Indian Ocean and along the climatological convergence zones in the Pacific. With the exception of AM3-CTL, all simulations also underestimate rainfall in the east Indian Ocean just south of the equator, where the MJO is most active (Salby and Hendon 1994; Wheeler and Kiladis 1999; Sobel et al. 2010). Numerous studies have demonstrated that an important link exists between the mean state and the MJO in GCM simulations (Inness et al. 2003; Zhang et al. 2006; Kim et al. 2011).

MJO-filtered precipitation variance increases dramatically in the GCM versions with modified treatments of deep convection (Fig. 2). To obtain Fig. 2, we filter precipitation anomalies to retain only eastward-propagating signals with zonal wavenumbers 1–6 and periods 20–100 days, and variances are then computed. Figure 2 indicates that the strongest increases in intraseasonal rainfall variance tend to occur near wet biases in the mean state (see Fig. 1, Kim et al. 2011). Large increases in variance are seen over both the west Pacific and Indian Oceans in the modified convection runs.

The raw spectral power of the equatorially symmetric component of tropical rainfall is displayed in Fig. 3. These plots are made using the methodology of Wheeler and Kiladis (1999) and are adapted from Fig. 6 in Benedict et al. (2013) with the addition of results for the CAM and SPCAM. Figure 3 shows that our modifications to the treatment of deep convection (as well as other processes, for the SPCAM) not only uniformly enhance low-frequency variability but also, more importantly, improve the distribution of spectral power by shifting the peak from westward- to eastward-propagating disturbances. AM2-TOK overestimates power in the MJO spectral range (here, defined as zonal wavenumbers +1 to +3 and periods 30–96 days), while MJO power is more realistic in AM3-A (Fig. 3e), but it is

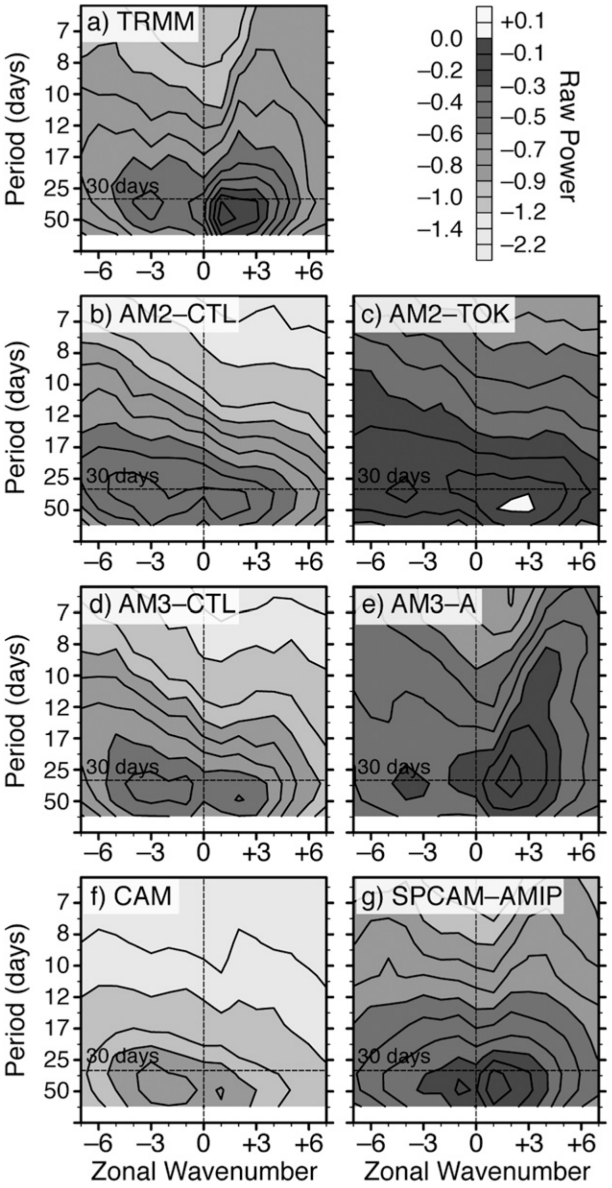

FIG. 3. Frequency–zonal wavenumber power spectra of the symmetric component (about the equator) of precipitation for (a) TRMM and (b)–(g) the GCM simulations. Displayed is the base-10 logarithm of the summation of power between 15°S and 15°N.

at a higher frequency (~30 days) than in observations (~45 days). SPCAM generates a realistic distribution of rainfall spectral power associated with the MJO (Fig. 3g), as shown in previous studies (Khairoutdinov et al. 2005; Benedict and Randall 2007). Of the modified GCMs examined here, the spectral pattern of eastward-moving tropical disturbances is best depicted by SPCAM.

In Fig. 4, we lag correlate U_{850} with an index time series of equatorial rainfall based at either 90° (left) or 150°E (right). All anomalies are 20–100-day bandpass filtered prior to correlation. Following the spectral distributions of Fig. 3, all control simulations produce disturbances that are highly inconsistent with observations (Figs. 4a,b). Although a well-defined signal moving eastward at the correct speed is noted in the west Pacific in AM2-TOK (Fig. 4f), this model only produces a weak and localized disturbance in the east Indian Ocean without clear eastward movement (Fig. 4e). Compared to AM2-TOK, AM3-A depicts a stronger and more coherent MJO signal in both ocean basins, but the simulated MJO phase speed is too fast in the west Pacific (Benedict et al. 2013). The apparent signal of westward-moving equatorial Rossby waves in the Indian Ocean is overemphasized in AM3-A compared to observations. SPCAM is able to reproduce observed MJO phase speeds in both ocean basins, but correlations are lower than those seen in nature. Our overall impression from Figs. 3 and 4 is that, compared to ERA-Interim, all modified GCMs simulate the MJO reasonably well in the west Pacific. In the Indian Ocean, only AM3-A and SPCAM are able to simulate the MJO eastward propagation to any degree, but even those have significantly weaker correlations than do the observations.

b. *Time-mean advective components of GMS*

In Fig. 5 we present, from top to bottom, boreal winter means of the horizontal ($T_R[\mathbf{v}\cdot\nabla s]$), vertical $\{T_R[\omega(\partial s/\partial p)]\}$, and total $\{T_R[\mathbf{v}\cdot\nabla s+\omega(\partial s/\partial p)]\}$ components of column-integrated moist entropy export derived from ERA-Interim. In each panel, thin and thick black lines represent the 3 and 6 mm day^{-1} precipitation contours, respectively. Horizontal advection exports column moist entropy $[s]$ (Fig. 5a) for all rainy regions of the tropical Indo-Pacific area. Vertical advection tends to weakly export $[s]$ where mean Indo-Pacific rainfall is greatest, from the eastern Indian Ocean to the SPCZ in the west Pacific. An import of $[s]$ by vertical circulations is seen along the central eastern Pacific ITCZ. Overall, $[s]$ export is strong and dominated by horizontal advection in the Indo-Pacific warm pool but near zero along the eastern Pacific ITCZ owing to a counteracting import by vertical circulations. Previous studies have examined annual-mean, column-integrated moist static energy export using a variety of reanalysis data sources (with different moist physics parameterizations), spatial grids, and analysis techniques (e.g., Back and Bretherton 2006; Peters et al. 2008). Our annual mean $[s]$ export plots (not shown) are consistent with those reported previously and give us confidence that the results of Fig. 5 are reasonably accurate.

A comparison of winter-mean and meridionally averaged terms related to NGMS is shown in Fig. 6. Meridional averaging is computed using a dynamic latitude

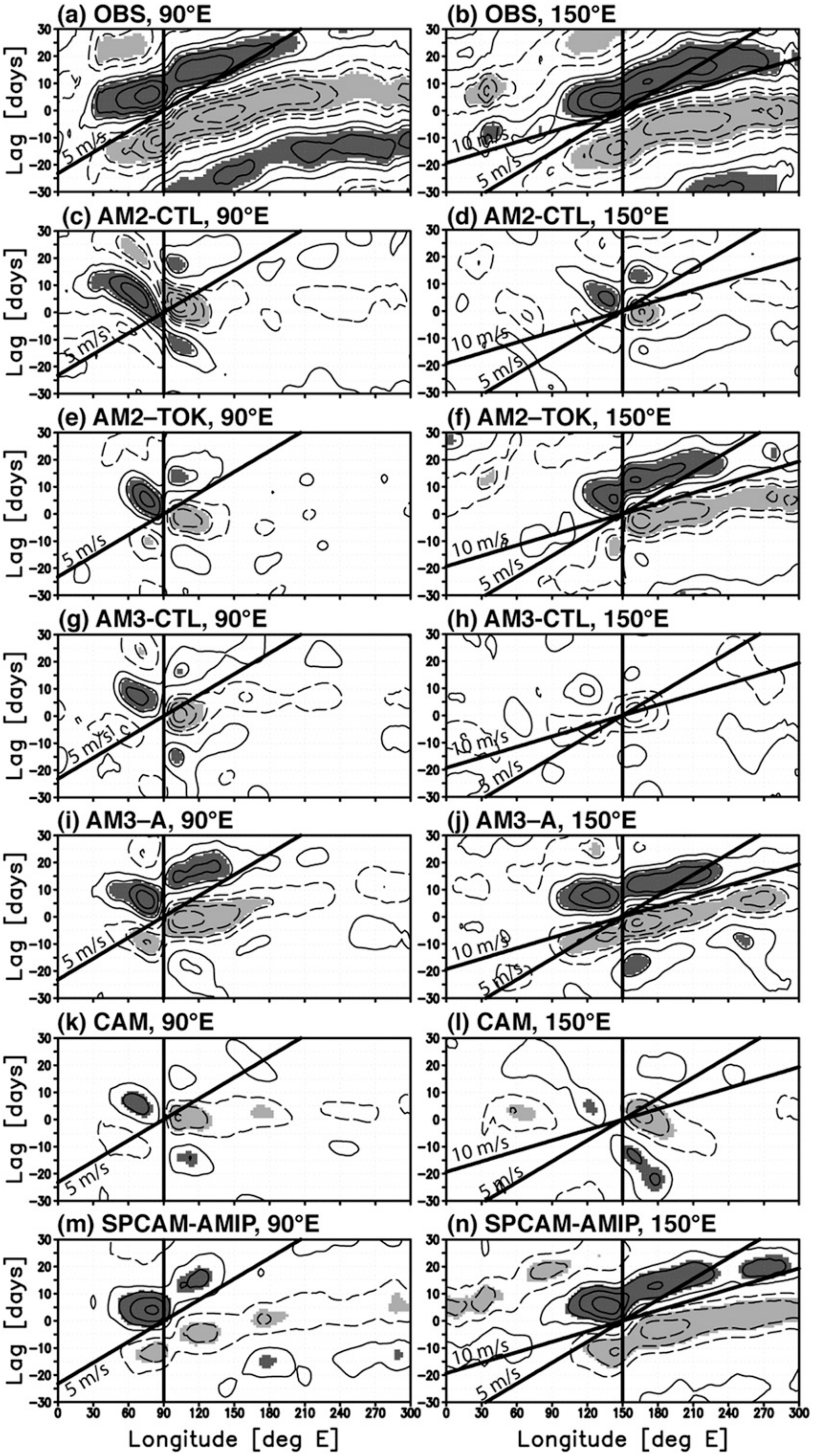

FIG. 4. Lag correlations of U_{850} with precipitation at (left) 90°E and (right) 150°E. Fields are 20–100-day filtered, averaged between 15°S and 15°N. Solid (dashed) contours represent positive (negative) correlations that are shaded dark (light) gray if they exceed the 95% statistical significance level. Observed wind and rainfall fields are taken from ERA-Interim and TRMM, respectively. In the left panels, index reference longitudes and the $5\,\mathrm{m\,s^{-1}}$ phase speed are marked by vertical and slanted thick lines, respectively. The right panels also contain the $10\,\mathrm{m\,s^{-1}}$ phase speed line.

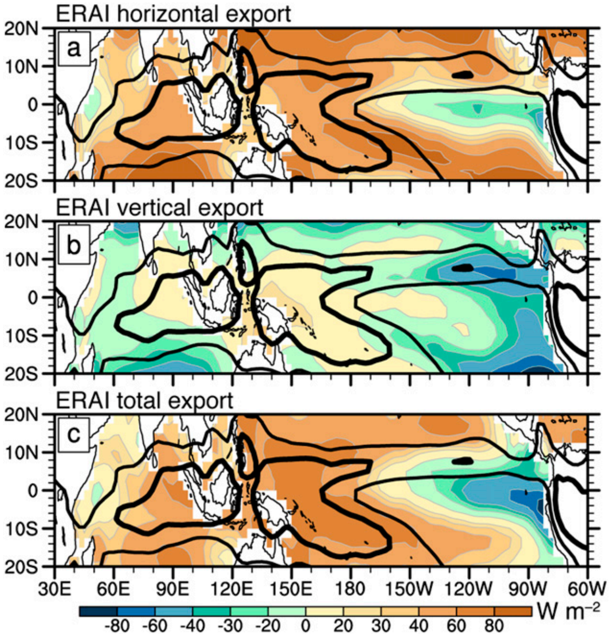

FIG. 5. ERA-Interim boreal winter-mean (a) horizontal $T_R[\mathbf{v}\cdot\nabla s]$, (b) vertical $T_R[\omega\partial s/\partial p]$, and (c) total $T_R[\mathbf{v}\cdot\nabla s+\omega\partial s/\partial p]$ column-integrated moist entropy export, shown in color shading. In all panels, thin (thick) contours represent the 3 (6) mm day^{-1} mean precipitation.

mask that includes only oceanic grid points where winter-mean vertically integrated moisture convergence (VIMC) is positive. We restrict the latitudinal bounds to be at most 15° from the equator. This meridional bounding (referred to as the climatological deep convection latitude band) can be approximated by the 3 mm day^{-1} contour of mean rainfall and effectively defines areas in each dataset where climatological deep convection occurs. Our results are not qualitatively sensitive to whether we choose to use a fixed (e.g., 15°S–10°N) or dynamic latitude range. In Fig. 6, two passes of a 1–2–1 filter have been applied in longitude prior to plotting. Compared to their corresponding control GCM simulations (dashed lines), each modified simulation (solid gray lines) produces a stronger winter-mean $[s]$ export by horizontal circulations (top row) but consistently stronger $[s]$ import (or weaker $[s]$ export) by vertical circulations (second row). Total $[s]$ export (third row) in the modified simulations—those with stronger MJOs—may be either stronger or weaker than total $[s]$ export in the control runs depending on whether the horizontal or vertical exports are dominant.

Longitudinal profiles of the winter-mean horizontal, vertical, and total components of NGMS (denoted by Γ_H, Γ_V, and Γ_T in Fig. 6, respectively) reveal a consistent theme for all models: compared to their respective control runs, a reduction in Γ_T, seen in each modified simulation (dashed black), is driven exclusively by a strong reduction in Γ_V, while Γ_H values in the modified simulations are similar to or slightly higher than those in the control runs (solid gray). Strongly reduced magnitudes of Γ_V and Γ_T occur for all longitudes even in the presence of a diverse distribution of column-integrated moisture convergence $\{-L[\nabla\cdot(r\mathbf{v})]$; second row from bottom$\}$ that in the modified simulations may be stronger (e.g., in the west Pacific) or weaker (e.g., near the Maritime Continent) than their respective control runs. These smaller positive values of Γ_T seen in each modified simulation increase the sensitivity of time-mean precipitation to a given entropy forcing, as in (2). Figure 6 clearly suggests that changes made to the treatment of deep convection that improve MJO strength in the three GCMs analyzed are closely linked to the behavior of time-mean NGMS in those models and that for each model these deep convective parameterization changes resulted in a strong reduction in Γ_T that is driven exclusively by strong negative tendencies in Γ_V.

c. Behavior of advective GMS components on intraseasonal scales

The relationship between winter-mean Γ_V and one measure of the robustness of MJO eastward propagation is shown in Fig. 7. The Γ_V values represent spatial averages within the climatological deep convection latitude band and between 50°E and 150°W. The MJO metric used here is nearly identical to the level-2 diagnostic from Waliser et al. (2009) and Kim et al. (2009) and is defined as the ratio of east–west raw spectral power of the component of annual tropical rainfall that is symmetric about the equator, where eastward signals represent the sum of power within the MJO spectral region of zonal wavenumbers +1 to +3 and periods 30–96 days while their westward counterparts are bounded by zonal wavenumbers −1 to −3 in the same range of periods. Figure 7 shows a coherent linear relationship between Γ_V and the MJO metric in which each simulation that produces a better MJO has both a more negative Γ_V value and a more positive east–west ratio. A similar relationship between the MJO metric and Γ_T is noted (pooled best-fit slope $m=-2.9$, $r=-0.92$; plot not shown), although the linear pattern shifts to higher Γ_T values where modified simulations loosely cluster around +0.17 while control simulations cluster around +0.32. No clear relationship exists between the MJO metric and Γ_H, (pooled best fit $m=+1.9$, $r=+0.41$). This suggests that the vertical rather than the horizontal time-mean NGMS component is more closely tied to total NGMS variations and appears to play a more significant role in determining the model's ability to

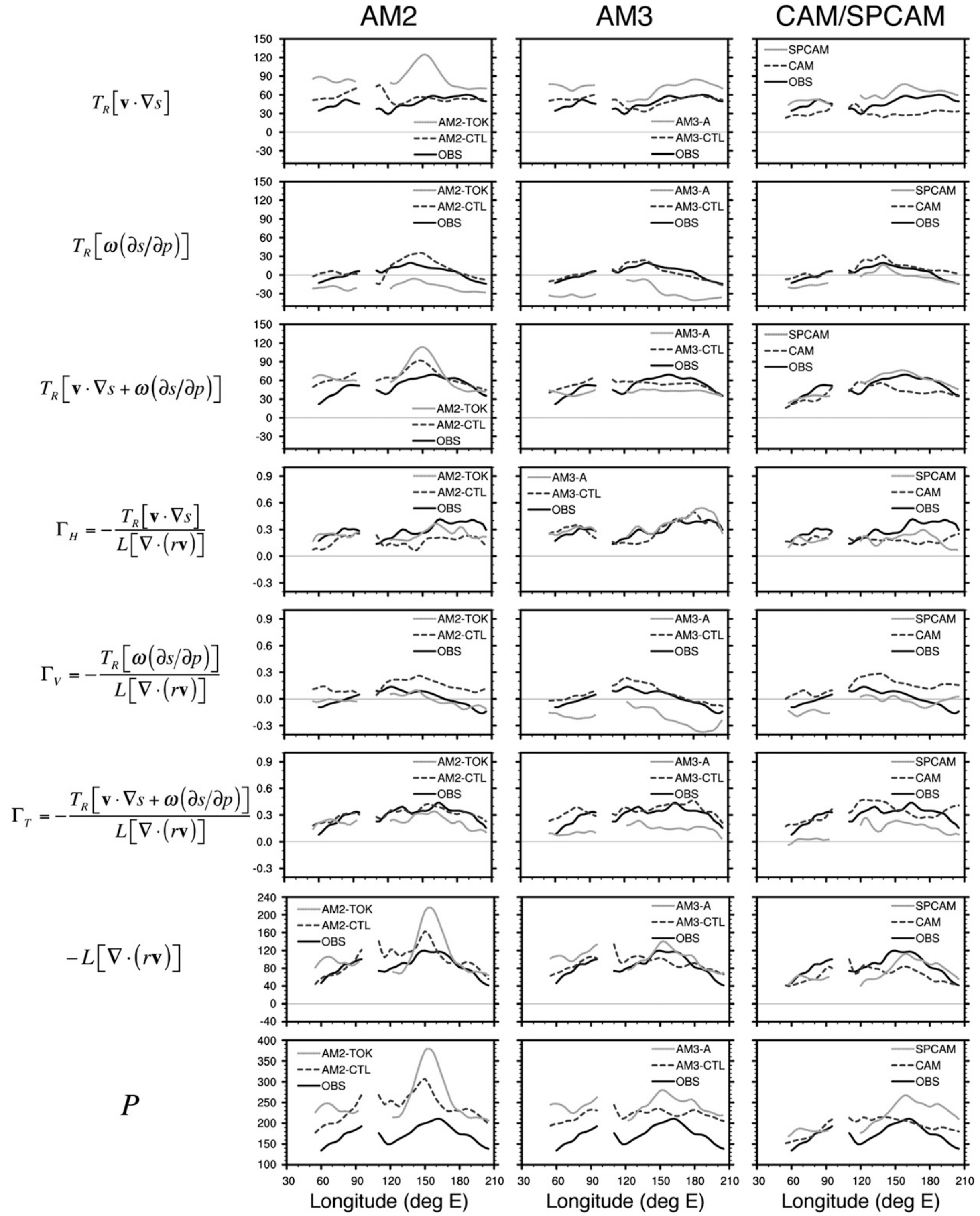

FIG. 6. Boreal winter means of selected advective and diabatic terms related to GMS in the (left)–(right) AM2, AM3, and CAM/SPCAM. Variables have been latitudinally averaged over a chosen Indo-Pacific domain where climatological vertically integrated moisture convergence is positive (see text). In each panel, solid black, dashed black, and gray lines represent observations, the control simulation, and the modified simulation, respectively. Variables shown are (top)–(bottom) horizontal, vertical, and total GMS advection terms ($\mathrm{W\,m^{-2}}$); their counterparts normalized by column moisture convergence (unitless); column moisture convergence ($\mathrm{W\,m^{-2}}$); and precipitation ($\mathrm{mm\,day^{-1}}$).

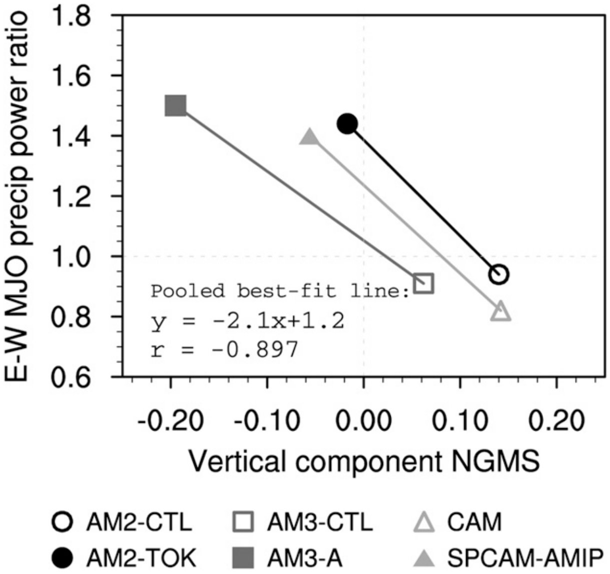

FIG. 7. The relationship between boreal winter-mean Γ_V and one metric of the robustness of MJO eastward propagation. The MJO metric is the ratio of eastward to westward tropical rainfall power within the MJO spectral region [periods 30–96 days, zonal wavenumbers +1 to +3 (eastward) or −1 to −3 (westward)]. Also shown are the equation and correlation coefficient r for the best-fit line of the pooled data points (pooled best-fit line not plotted).

realistically simulate the MJO. Figure 7 is an exercise in understanding possible connections between NGMS and the MJO in the GCM simulations, so we omitted the point based on ERA-Interim. The location of the reanalysis point ($\Gamma_V = +0.01$, E : W ratio = +2.4) falls well off the pooled best-fit line and suggests that, acknowledging the uncertainties of the reanalysis dataset, some deficiencies in the simulated relationship between deep convection and the large-scale circulation remain. Factors other than time-mean GMS such as rain-intensity-dependent moisture distributions may also affect the MJO (Kim et al. 2014b).

We now examine how NGMS varies as a function of convective activity, with implications for NGMS variations during MJO events. Figure 8 shows scatterplots of the vertical $\{T_R[\omega(\partial s/\partial p)]\}$ and horizontal $(T_R[\mathbf{v}\cdot\nabla s])$ components of moist entropy divergence versus VIMC $\{-L[\nabla\cdot(r\mathbf{v})]\}$. Each dot represents a daily value spatially averaged over the east Indian Ocean (10°S–5°N, 70°–100°E). Scatterplots using equatorial west Pacific data (omitted) are qualitatively similar to Fig. 8. The results for ERA-Interim indicate that horizontal advection nearly always works to reduce column s in moist regions regardless of the sign or magnitude of VIMC. However, vertical advection is significantly correlated with VIMC such that s divergence owing to vertical advection increases with increasing VIMC. Conversely, when convective intensity is weaker (i.e., negative or weakly positive VIMC), vertical advection can contribute to convergence of s into the column. We hypothesize that the behavior seen in the ERA-Interim vertical advection component may be related to cloud regime fluctuations on subseasonal scales. Presumably, strongly positive VIMC represents regions of mature cumulonimbi and their associated abundant stratus clouds that are effective at reducing column s. Weakly positive VIMC likely represents areas of shallow cumuli or congesti, whose circulations can increase column s as noted in Fig. 8, consistent with previous observational analyses (e.g., Haertel et al. 2008). Each control simulation—one that produces unrealistically weak intraseasonal variability—qualitatively reproduces the general relationship between s divergence and VIMC (Fig. 8, left). Strikingly different behavior is noted in the simulations that have more intense MJOs (Fig. 8, right). In both AM modified runs, horizontal advection exports column s but is a strongly increasing function of VIMC—in contrast to the control simulations and ERA-Interim. Unlike ERA-Interim, vertical advection is not an increasing function of VIMC and is mostly involved in s import, even for large VIMC. Thus, when VIMC is strongly positive in the presence of vigorous deep convection, vertical circulations still converge s into the column while horizontal advection does all of the "heavy lifting" to export the excess s. We note that vertical advection in the west Pacific (not shown) shows a greater tendency for s divergence but is insensitive to VIMC for AM2-TOK and AM3-A. Interestingly, SPCAM is better able to reproduce the key advective features seen in the ERA-Interim plot, including the insensitivity of horizontal advection to VIMC and the positive slope of the vertical advection–VIMC line. The toy model of Raymond and Fuchs (2009), which produces robust MJO-like disturbances, depicts relationships between s divergence and VIMC that are similar to the results for AM2-TOK and AM3-A. A more detailed discussion on the different relationships between VIMC and entropy advection in the GCMs will be presented in section 5.

Figures 6–8 suggest that vertical advection plays an important role for the MJO on time-mean scales and as convective intensity fluctuates by importing column-integrated s during periods of relatively weak moisture convergence. Given that VIMC is, on average, positive in the MJO active regions even during its suppressed phase (not shown), (5) indicates that the sign of Γ_V is determined by $[\omega(\partial s/\partial p)]$. In Fig. 9 we display profiles of s and normalized pressure velocity $-\omega$ averaged over the equatorial east Indian Ocean region (85°–95°E) only during MJO suppressed conditions. We define the

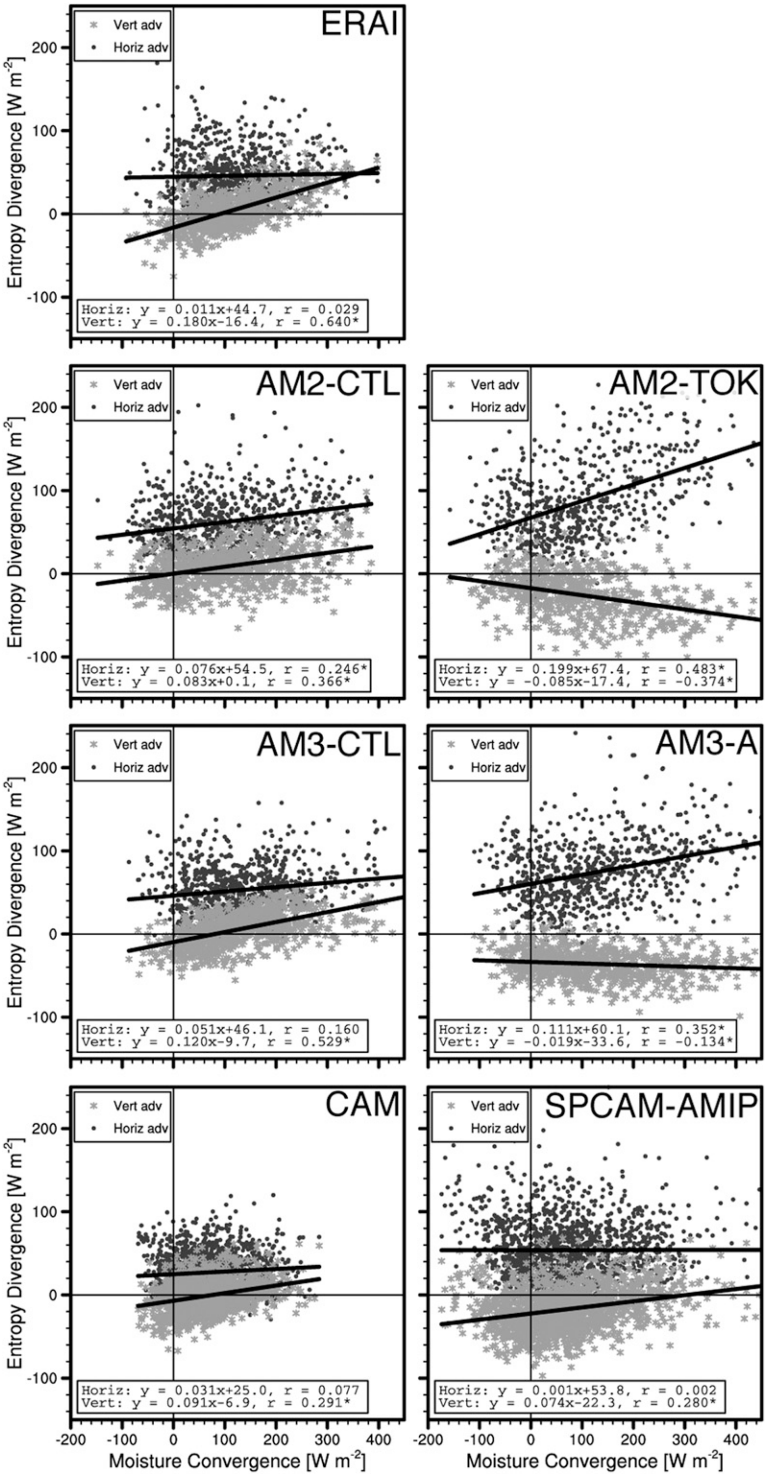

FIG. 8. Horizontal (dark bullets) and vertical (asterisks) advective components of vertically integrated moist entropy divergence vs VIMC averaged over the east Indian Ocean region during boreal winter. Conditional sampling has been done to include only times when the 91-day windowed variance of a precipitation index is greater than its winter average value. Land points are omitted from the spatial averages. Each point represents a single day. Thick black best-fit lines are overlaid, and the corresponding equations and correlation coefficients *r* appear at the bottom of each panel. Asterisk *r* values are statistically significant above the 95% confidence level.

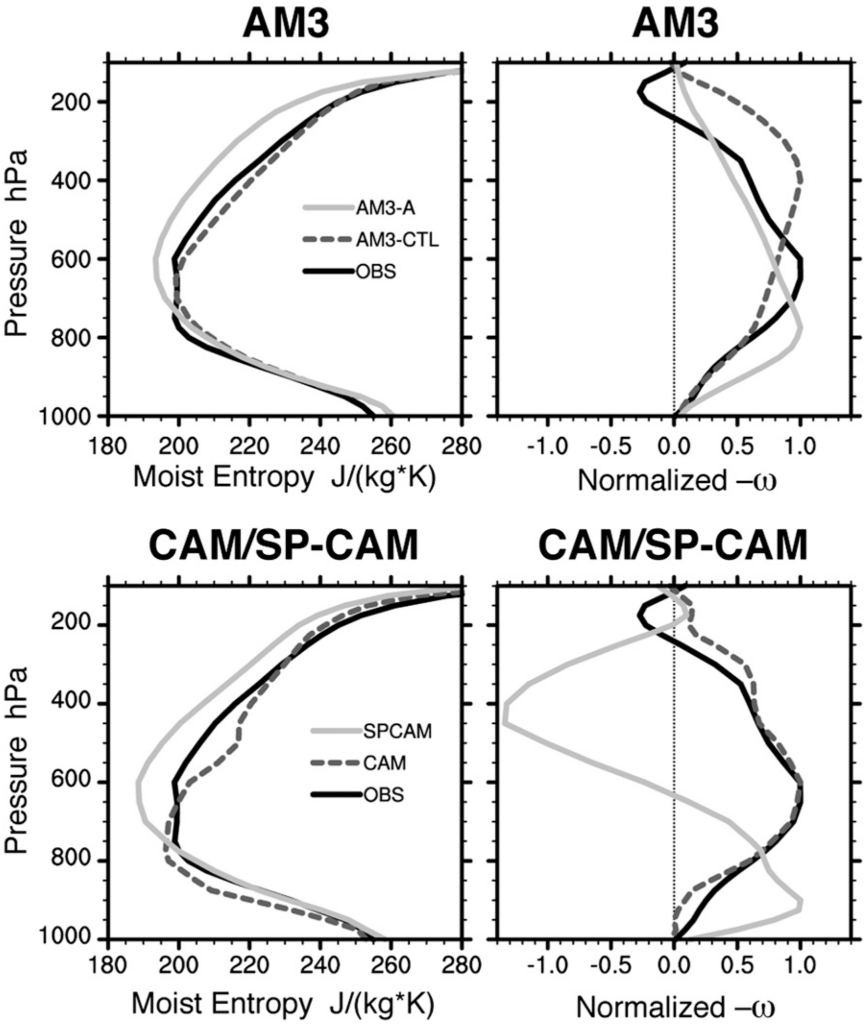

FIG. 9. MJO suppressed-phase profiles of (left) moist entropy s and (right) pressure velocity $-\omega$ normalized by the value of peak upward motion for (top) AM3 and (bottom) CAM/SPCAM simulations. Profiles are conditionally averaged over the equatorial east Indian Ocean (85°–95°) to include only those days during boreal winter in which a MJO rainfall index is less than -1σ.

suppressed phase as boreal winter days when 20–100-day filtered and standardized east Indian Ocean rainfall is less than -1σ. Because this threshold captures some lightly raining situations, the $-\omega$ profiles are weakly positive, and this behavior is magnified by the normalization. Profiles for the convectively active phase are omitted because, for all data sources, $-\omega$ shows a "top heavy" profile with a maximum near 350 hPa, the minimum in s occurs at a much lower level (~600–750 hPa), and therefore vertical circulations effectively export s out of the column (see Raymond et al. 2009). Larger differences among the simulations are noted during the MJO suppressed phase. For brevity, we focus on the two models with the largest amount of intraseasonal variability in the tropical Indian Ocean: the AM3 and SPCAM (cf. Fig. 4). Qualitatively similar s profiles are seen among the AM3 profiles, but AM3-A produces a more realistic lower- to midtropospheric peak in $-\omega$ (Fig. 9b). For AM3-A, $-\omega$ is larger where $\partial s/\partial p$ is positive and smaller where $\partial s/\partial p$ is negative, yielding negative Γ_V and thus s import. In AM3-CTL, however, $-\omega$ is weighted more heavily toward the upper troposphere and exhibits a peak well above the minimum in s (Fig. 9a), resulting in positive Γ_V and s export. Slightly different behavior is noted in the CAM–SPCAM comparison, although the end result is the same. Although the CAM $-\omega$ maximum matches ERA-Interim (Fig. 9d), its s minimum occurs at a much lower pressure level (Fig. 9c). Thus, $-\omega$ is weak where $\partial s/\partial p$ is positive at low levels in CAM, while $-\omega$ is stronger where $\partial s/\partial p$ becomes negative aloft, yielding positive Γ_V that contributes to s export. The SPCAM $-\omega$ profile is clearly different than that in CAM and, combined with a minimum of s at a higher pressure level, produces sharply negative Γ_V and s import.

Further exploring intraseasonal fluctuations of NGMS, we present lagged linear regressions of both anomalous and total NGMS in Fig. 10. The index used is a time series of equatorial, MJO-filtered, and standardized precipitation at 90°E. The plots represent the temporal behavior of the NGMS components associated with a $+1\sigma$ change in the MJO rainfall index. In ERA-Interim, both horizontal and vertical NGMS components are positively correlated with Γ_T, but Γ_V leads Γ_T by 3–7 days while Γ_H lags Γ_T by ~1–5 days (Fig. 10, top left). The negative Γ_T tendencies about 2–3 weeks prior to peak convection are initially driven by Γ_V and are likely associated with the shallow cumulus and congestus regime that imports s. Negative Γ_H lags the Γ_T minimum but sustains s import longer than if Γ_V were acting alone. As peak convection develops near day 0, Γ_V drives a rapid shift to positive Γ_T, the stratiform cloud regime emerges, and export of s begins. The peak of Γ_H again lags Γ_T by a few days and is consistent with strong low-level anomalous divergence linked to the westerly wind bursts, Rossby gyres, and enhanced mixing due to synoptic disturbances (Benedict and Randall 2007; Maloney 2009). Import of s—largely through negative Γ_V—redevelops 2–3 weeks after peak convection as the MJO suppressed phase returns. Notably, anomalous fluctuations of Γ_V and Γ_H are of approximately the same magnitude in ERA-Interim. Observed NGMS fluctuations in the equatorial west Pacific (not shown) have patterns similar to those in the east Indian Ocean but are of smaller magnitude.

The modified GCM simulations (Fig. 10, left) produce NGMS fluctuations that are qualitatively consistent with ERA-Interim despite signals that may be less robust statistically, while the control runs have weaker NGMS fluctuations and less realistic behavior. The modified simulations generally foster larger fluctuations in NGMS anomalies, particularly those related to Γ_V, compared to the control runs. In AM3-CTL and CAM, fluctuations of Γ_T are almost entirely driven by Γ_H while Γ_V plays a much smaller role. Similar behavior is noted in both AM2-CTL and AM2-TOK (omitted), reaffirming the poor east Indian Ocean MJO signal in those models (Fig. 4). The interplay of NGMS components is better captured in AM3-A—the version of AM3 that produces a more realistic MJO.

The right column of Fig. 10 shows the regressed form of the NGMS components with their respective mean values included. Fluctuations associated with NGMS anomalies can represent large percentages of the background NGMS. For example, the typical peak-to-trough difference of ~0.18 for Γ_T in ERA-Interim (Fig. 10, top left) is about 45% of the background value of ~0.40 estimated by averaging Γ_T in the top-right ERA-Interim panel of Fig. 10 across all lag days. We obtain similar results for ERA-Interim Γ_H, but for Γ_V, the fluctuations (~0.11) are larger than the background value itself (~+0.05). Importantly, the fluctuating part of Γ_V is large enough to shift total Γ_V to values that are near zero or slightly negative during the MJO suppressed phase, which is consistent with Haertel et al. (2008). The NGMS fluctuations relative to the background NGMS in the GCM simulations varies widely. Anomaly fluctuations of Γ_T and Γ_H constitute anywhere from 15% (AM3-CTL) to 150% (SPCAM) of the background values. The fluctuating components represent larger percentages of the background NGMS in the models that produce more realistic MJOs (in Fig. 10, AM3-A and SPCAM). In none of the simulations are the magnitudes of NGMS fluctuations large enough to change the sign of the background NGMS value over the MJO lifetime, perhaps suggesting that the background NGMS magnitude and sign of the various NGMS components—rather than the intraseasonal anomalies of these components—may be dominant in determining an MJO instability mechanism related to NGMS.

d. *Intraseasonal moist entropy budget*

Following Neelin and Held (1987) and Maloney (2009), the budget of vertically integrated and 20–100-day bandpass-filtered s may be written

$$T_R[\partial s/\partial t]_{\text{ISO}} = -T_R([\omega \partial s/\partial p]_{\text{ISO}} + [\mathbf{v}\cdot\nabla s]_{\text{ISO}}) + \text{LH}_{\text{ISO}} + \text{SH}_{\text{ISO}} + [\text{LW}]_{\text{ISO}}. \qquad (6)$$

In (6), subscript ISO signifies that variables have been 20–100-day bandpass filtered; LH and SH are the surface latent and sensible heat fluxes, respectively; and LW is the longwave heating rate. Other notation is the same as in previous equations. We omit negligible contributions to the s budget from $[\text{SW}]_{\text{ISO}}$. Budget anomaly residuals are, at most, $7\,\text{W}\,\text{m}^{-2}$ for ERA-Interim, AM2-CTL, CAM, and SPCAM; $2\,\text{W}\,\text{m}^{-2}$ for the AM3 runs; and $20\,\text{W}\,\text{m}^{-2}$ for AM2-TOK. The first term in (6) represents the column-integrated time tendency of s, and the second and third terms are the column-integrated export of s due to vertical and horizontal advection, respectively. Figure 11 shows the s budget terms in (6) and the precipitation anomaly composited based on all local maxima between the months of September and April that exceed $+1\sigma$ in an ISO-filtered and standardized equatorial east Indian Ocean precipitation

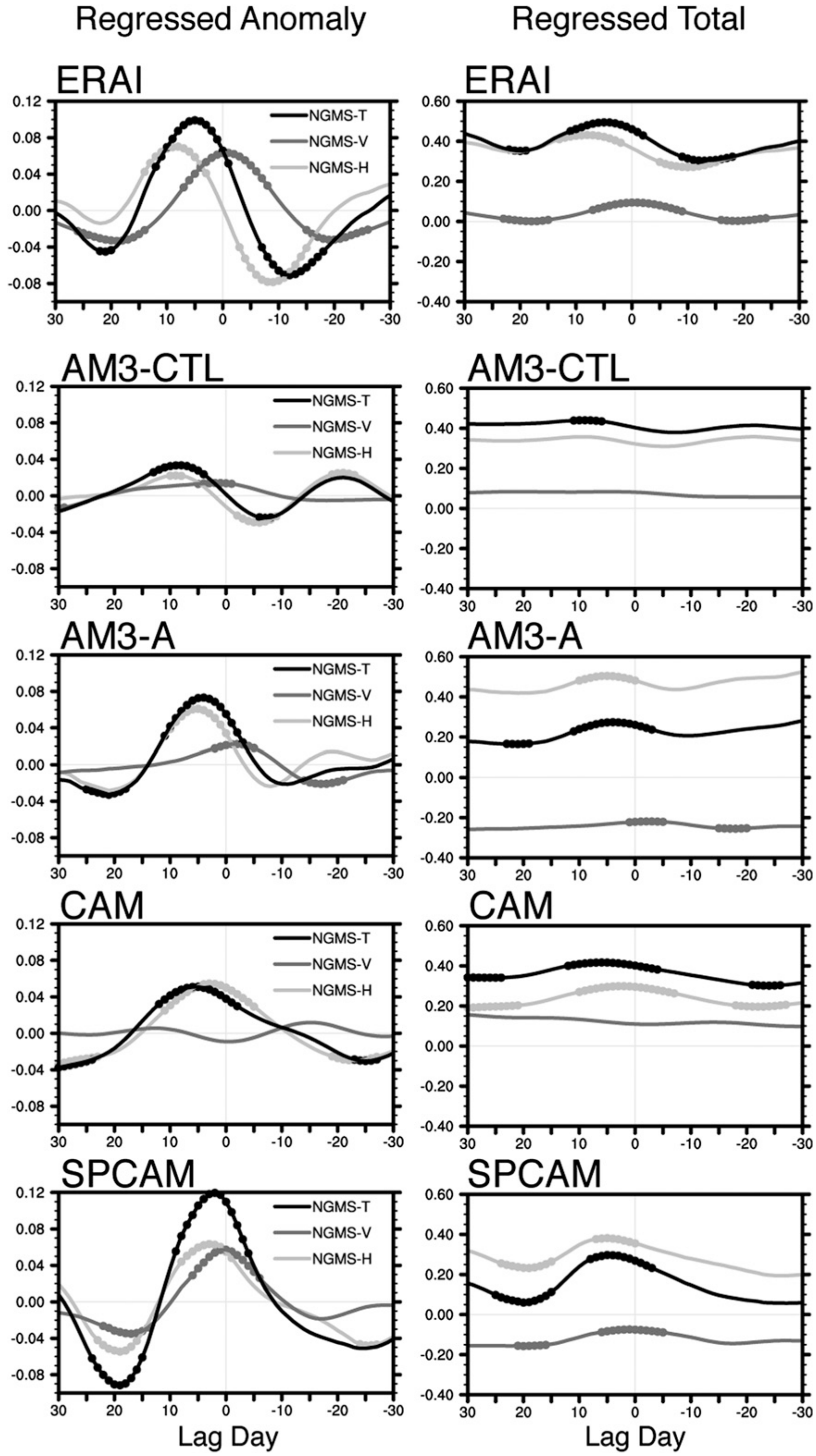

FIG. 10. The 20–100-day bandpass-filtered (left) anomalous and (right) total NGMS linearly regressed onto an MJO precipitation index at 90°E. Each plot shows the total (NGMS-T, or Γ_T), vertical (NGMS-V, or Γ_V), and horizontal (NGMS-H, or Γ_H) components of NGMS. Regressed variables have been averaged to include only those latitudes where climatological VIMC is positive (see text). Dotted line sections denote values that are statistically significant above the 92.5% level. Negative lag days occur before maxima in the MJO rainfall index.

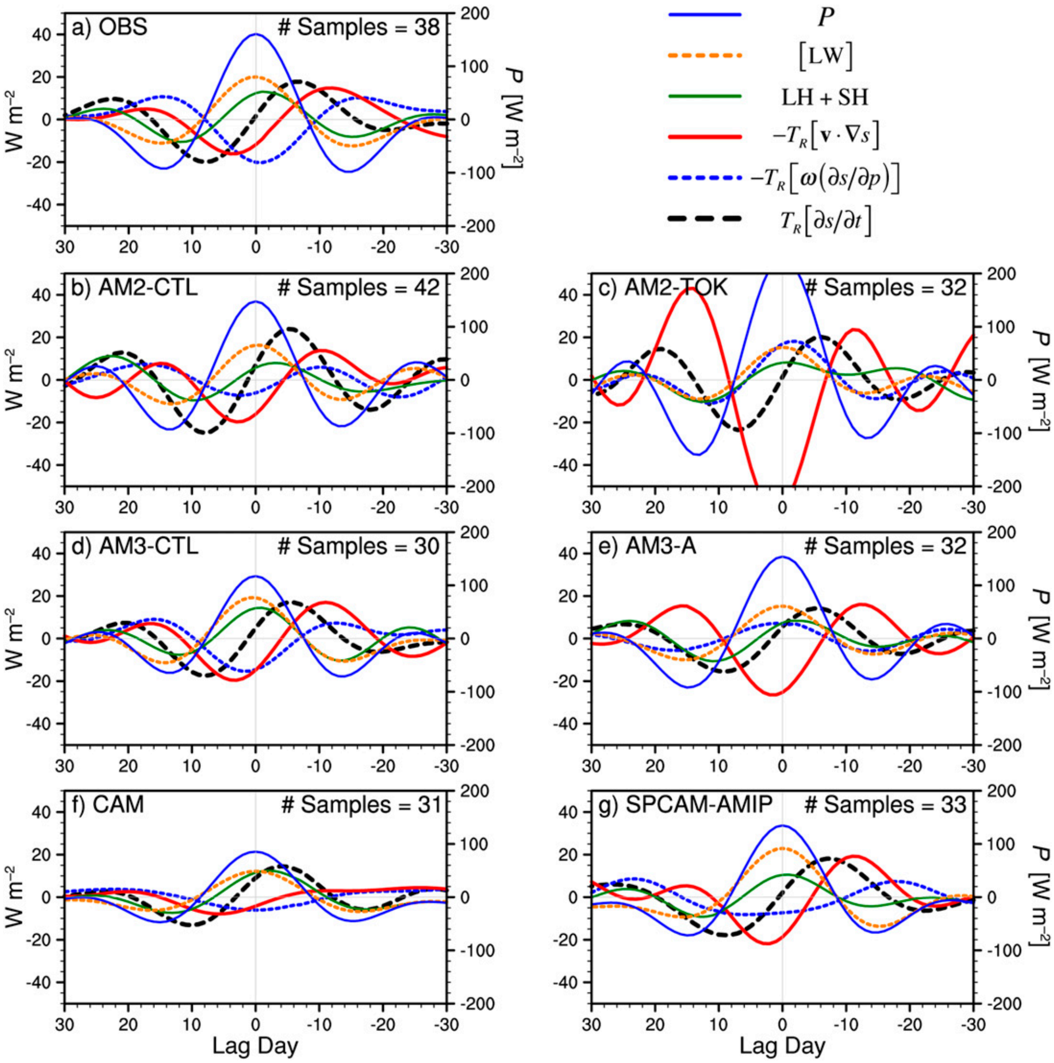

FIG. 11. Budget of equatorial (15°S–10°N) moist entropy based on a composite of September–April MJO events in the east Indian Ocean for (a) ERA-Interim/TRMM and (b)–(g) GCM simulations. All variables are 20–100-day filtered and are shown in energy units (W m^{-2}). The left y axis scale is for terms contributing to the moist entropy budget, and the right y-axis scale is for precipitation P. Negative days occur before the MJO peak rainfall. Composite sample sizes appear at the upper right of each panel. See text for further details.

index. Our findings are qualitatively similar for MJO events in the west Pacific Ocean (not shown). For all datasets, the s time tendency term leads precipitation by 90°, where column s accumulates during anomalously dry periods and is exhausted during heavy rainfall. In ERA-Interim (Fig. 11a), the advection terms are roughly 180° out of phase with LH, [LW], and precipitation. Consistent with the results of Fig. 10, an increase of [s] 1–3 weeks ahead of peak rainfall is associated with both vertical and horizontal advection in ERA-Interim (Fig. 11a). During heaviest rainfall, [LW] and LH contribute strongly to positive time tendencies of [s] while advection attempts to reduce [s]. These temporal patterns of the s budget are reminiscent of the moist static energy budget composites reported in Kiranmayi and Maloney (2011).

All simulated patterns of [$\partial s/\partial t$] (Figs. 11b–g) are qualitatively consistent with ERA-Interim despite differences in the dominant terms on the rhs of (6). Both AM2-CTL and AM3-CTL (Figs. 11b,d) produce budget patterns similar to ERA-Interim, but in the corresponding modified simulations (Figs. 11c,e) vertical advection contributes to positive time tendencies of [s] during heaviest rainfall, in contrast to both control runs, ERA-Interim, and SPCAM. The positive correlation between vertical advection and precipitation is presumably what promotes a reduced NGMS in the modified AM runs and is also consistent with Fig. 8. The unrealistic behavior in vertical advection working to increase $[s]$ is offset by weaker LH and [LW] and an enhanced negative contribution from horizontal advection, especially for AM2-TOK. Owing to the unrealistic advective tendencies in AM2-TOK (and perhaps AM3-A), we question whether the stronger intraseasonal variability in that model is being produced for reasons that are physically consistent with intraseasonal variability seen in ERA-Interim. Small horizontal and vertical advective tendencies result in unrealistically weak fluctuations in CAM (Fig. 11f). The s budget terms are reproduced well in the SPCAM (Fig. 11g), with the import of $[s]$ ahead of peak MJO rainfall driven initially by vertical advection and subsequently horizontal advection as in ERA-Interim (Fig. 11a).

5. Summary and discussion

This study reviews differences in normalized gross moist stability (NGMS) seen in a comparison of three pairs of GCMs. In each GCM pair, one member produces weak intraseasonal variability while the other produces stronger intraseasonal variability and more realistic MJO disturbances owing to a modification in the treatment of deep convection. The assessment of NGMS and its horizontal and vertical advective components is of interest because of the demonstrated link between NGMS and moisture modes—convectively coupled disturbances that resemble the MJO and whose development and dynamics in reduced-complexity models are closely linked to moisture perturbations (e.g., Sobel et al. 2001; Fuchs and Raymond 2005; Sugiyama 2009). Moisture mode instability in these models occurs when NGMS—or effective NGMS when accounting for additional diabatic sources—is negative. The results of this study do not prove or disprove any particular conceptual model of the MJO. Rather, they simply illustrate a systematic relationship between intraseasonal convective intensity and the behavior of the vertical NGMS advective component in selected GCM simulations and in the ERA-Interim.

A consistent picture emerges between models with weak intraseasonal variability (weak ISV) and those with strong intraseasonal variability and more realistic MJOs (strong ISV) in terms of their time-mean total, horizontal, and vertical NGMS components (Γ_T, Γ_H, and Γ_V, respectively). Compared to the control simulations, a reduction in winter-mean Γ_T in each modified simulation is driven by a substantial reduction in Γ_V, while Γ_H remains similar to or slightly higher than its control simulation value (Fig. 6). Values of Γ_T in the strong-ISV models are reduced from the values of their weak-ISV counterparts, while Γ_V shifts from weakly positive to negative. Our results show a highly correlated linear relationship between winter-mean and warm-pool-averaged Γ_V (or Γ_T) and the robustness of MJO eastward propagation in the models (Fig. 7). In the simulations examined, east-to-west ratios of power in the MJO spectral region increase as Γ_V decreases and becomes negative. No relationship exists between Γ_H and the MJO metric, suggesting that the time-mean vertical advective NGMS component is more closely tied to intraseasonal variability in the GCMs examined.

We also demonstrate connections between variations in NGMS and the MJO on subseasonal time scales. In the reanalysis, export of vertically integrated moist entropy ($[s]$) by vertical advection occurs when vertically integrated moisture convergence (VIMC) is positive and large, presumably in the presence of mature cumulonimbi and their associated stratus clouds (Fig. 8, top). For shallower convection, when VIMC is only weakly positive, import of s occurs. Horizontal advection in ERA-Interim exports $[s]$ but is an insensitive function of VIMC. On subseasonal scales, the relationship between column-integrated s advection and VIMC differs among the simulations examined and will be discussed further below.

The efficiency of s import as a means of gradually recharging column moisture during the suppressed MJO phase is model dependent and is effectively portrayed by viewing profiles of s and vertical pressure velocity $-\omega$ (Fig. 9). In AM2 (omitted) and AM3 (Fig. 9, top), the reduction in Γ_V and thus the stronger import of s in the modified simulations results from a more bottom-heavy ω profile, while the s profiles show similar patterns. For the CAM/SPCAM comparison, however, the shift of the s minimum to lower heights—despite a more realistic ω profile—results in a more negative Γ_V and stronger s export in CAM.

Total and anomalous NGMS undergo notable fluctuations during an MJO life cycle. During the MJO suppressed phase, negative Γ_T anomalies are driven initially by Γ_V and sustained by Γ_H (Fig. 10). During the MJO active phase, Γ_V drives positive anomalies of Γ_T that are again sustained by Γ_H. Fluctuations of anomalous NGMS components associated with the MJO can represent large fractions of the background NGMS magnitude, particularly for Γ_V. Anomalous NGMS indeed modulates the magnitude of background NGMS, but only for ERA-Interim Γ_V were these anomaly fluctuations large enough to change the sign of the total form of that NGMS component during the composite MJO. Additional diabatic sources may create an effectively negative NGMS even if background NGMS remains weakly positive (Su and Neelin 2002; Bretherton and Sobel 2002; Sugiyama 2009). A more rigorous analysis of the contributions to effective NGMS by these diabatic sources is deferred to future studies.

The composite MJO s budget underscores the critical role that advection plays in the accumulation of s ahead of peak MJO rainfall (Fig. 11). Fluxes of surface latent heating and vertically integrated longwave radiation are in phase with precipitation, suggesting that the advective tendencies are the primary drivers of changes in $[s]$ and precipitation. Consistent with the behavior of regressed NGMS components relative to the MJO (Fig. 10), vertical and then horizontal advection drive a positive time tendency of $[s]$, which itself leads positive precipitation anomalies. Unrealistic profiles of vertical advection are seen in AM2-TOK and to a lesser extent in AM3-A, but all budget terms in SPCAM closely match those in ERA-Interim.

The relationship between VIMC and vertical and horizontal exports of s differs among the GCM simulations examined (Fig. 8, bottom) and is worth additional discussion. That the AM2-CTL and AM3-CTL (and possibly CAM) distributions of entropy divergence versus convective activity more closely resemble ERA-Interim than those from the perturbed model versions with stronger MJOs is interesting. We propose two possibilities to explain this dilemma. One possibility is that the ERA-Interim advective tendencies are in error due to missing or incorrect physics in the reanalysis model. While we do not have access to ERA-Interim analysis increments that are generated in the process of data assimilation to reconcile the model state with observations, previous work with reanalysis datasets indicates that such analysis increments may be large in the context of MJO heat and moisture budgets. For example, Mapes and Bacmeister (2012) demonstrate that the Modern-Era Retrospective Analysis for Research and Applications has a large positive moisture budget analysis increment in the shallow convective phase of the MJO, suggesting a lack of deep convective restraint, which would also suggest that NGMS is too high during this period. Kiranmayi and Maloney (2011) also note a large positive residual in the moist static energy budget during the moistening phase of the MJO life cycle in ERA-Interim fields. Moist static energy advective tendencies in that study were calculated using standard model output variables, and analysis increments were not available.

Another possibility to explain differences between ERA-Interim and GCM entropy budgets is that AM3-A and AM2-TOK may be producing stronger intraseasonal variability for the wrong reasons. Figure 8 suggests that, even for high precipitation rates, vertical advection by divergent circulations imports moist entropy in the modified AM2 and AM3 simulations. Horizontal advection may compensate to maintain energy balance, which is reflected in a greater slope for horizontal entropy divergence in AM3-A and AM2-TOK relative to the control versions of these models (Fig. 8). Kim et al. (2011) demonstrated that models with stronger intraseasonal variability often have common mean-state biases, such as excessive mean precipitation in the off-equatorial west Pacific during boreal summer. These biases might reflect the need for the models to accomplish more energy transport to high latitudes by the rotational flow to compensate for unrealistic vertical advection. Interestingly, vertical advection in SPCAM transitions from importing to removing column s as moisture convergence increases, which matches the behavior seen in ERA-Interim (Fig. 8).

Although a clear relationship exists between intraseasonal variability and the winter-mean vertical advective components of gross moist stability, the behavior of GCMs examined here differs on subseasonal scales. Figures 8 and 11 reveal that during intense precipitation ERA-Interim, all control simulations, and SPCAM indicate that horizontal and vertical advection work together to reduce column s. In contrast, vertical circulations continue to import column s during heavy rainfall for strong-ISV versions of AM2 and (to a lesser extent) AM3. This same behavior is found in the toy model of Raymond and Fuchs (2009), which also produces robust MJO-like disturbances. Hannah and Maloney (2014) examined versions of CAM5 with different minimum entrainment rates for deep convective parameterization, akin to the methodology used here for AM2-TOK. Those authors discovered inconsistencies similar to those seen in Fig. 8 above and attribute the amplification of column-integrated advection as a response to unrealistically weak column radiation feedbacks. In a manner analogous to Fig. 8, scatterplots of anomalous column-integrated radiative heating versus moisture convergence indeed show that strong-ISV AM2 and AM3 versions have too-weak feedbacks between radiation and precipitation (Fig. 12). The balance of evidence from Figs. 8, 11, and 12 suggests that the modification of the deep convective parameterization used in AM2 and AM3 appears to produce more realistic intraseasonal variability but for reasons that are inconsistent with reanalysis. The overly intense vertical advective processes that import column moist entropy are balanced by (i) weaker radiative feedbacks (stronger radiative cooling to space) and (ii) overly intense horizontal advective processes that reduce column moist entropy. SPCAM produces improved intraseasonal variability without unrealistic changes in the

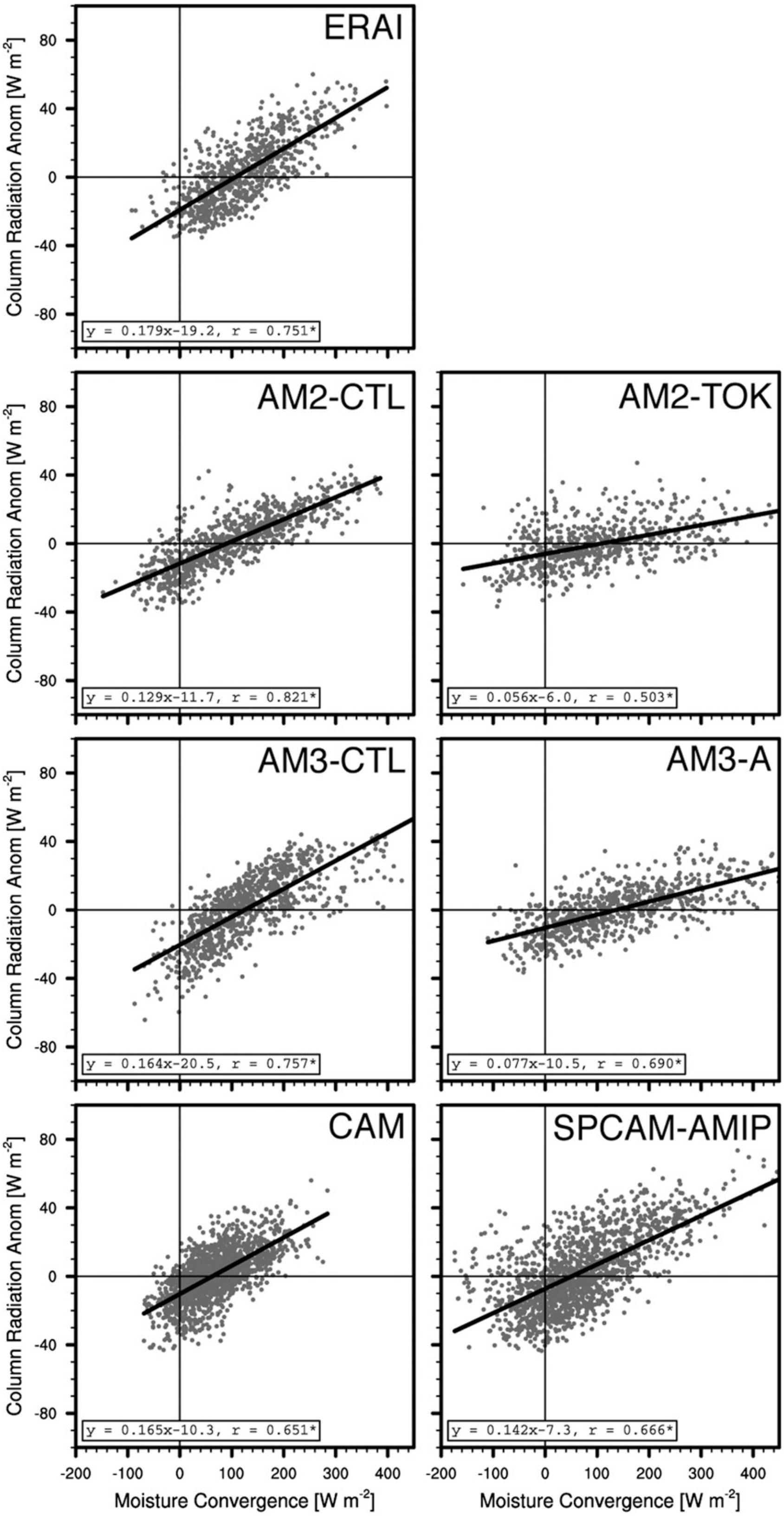

FIG. 12. As in Fig. 8, but for anomalous vertically integrated radiative heating.

relationships between moist entropy advection and radiative feedbacks.

We have demonstrated that the development of more robust MJO disturbances in GCMs with modified deep convection schemes is associated with reductions in total NGMS driven primarily by the vertical NGMS advective component rather than the horizontal advective component. Anomalous NGMS fluctuations associated with the MJO can strongly modulate the magnitude of background NGMS as well, although shifts from positive to negative values are only seen in the vertical NGMS component in the reanalysis dataset and not in any of the simulations examined. The sign of NGMS is primarily a function of the time mean, while its magnitude changes substantially during the passage of MJO disturbances. Exactly how the NGMS magnitude fluctuations might affect moisture mode instability and the MJO initiation and maintenance remains a topic of great interest. Additional research that examines the detailed role that surface moist entropy fluxes, cloud–radiative feedbacks, and other diabatic sources play in influencing vertically integrated moist entropy will also provide greater insight into the impact of effectively negative NGMS on the MJO.

Acknowledgments. We thank two anonymous reviewers for their constructive and insightful comments. We also thank David Raymond and the WGNE MJO Task Force for their scientific advice and motivation of this work. This work was supported by Awards NA08OAR4320893, NA12OAR4310077 (JJB, EDM) and NA08OAR4320912 (AHS) from the National Oceanic and Atmospheric Administration, U.S. Department of Commerce, and by the Climate and Large-Scale Dynamics Program of the National Science Foundation under Grants AGS-1025584, AGS-1062161, and AGS-1347738 (EDM). The statements, findings, conclusions, and recommendations do not necessarily reflect the views of NSF, NOAA, or the U.S. Department of Commerce.

REFERENCES

Adler, R. F., and Coauthors, 2003: The Version-2 Global Precipitation Climatology Project (GPCP) monthly precipitation analysis (1979–present). *J. Hydrometeor.,* **4,** 1147–1167, doi:10.1175/1525-7541(2003)004<1147:TVGPCP>2.0.CO;2.

Anderson, J. L., and Coauthors, 2004: The new GFDL global atmosphere and land model AM2–LM2: Evaluation with prescribed SST simulations. *J. Climate,* **17,** 4641–4673, doi:10.1175/JCLI-3223.1.

Arakawa, A., 2004: The cumulus parameterization problem: Past, present, and future. *J. Climate,* **17,** 2493–2525, doi:10.1175/1520-0442(2004)017<2493:RATCPP>2.0.CO;2.

Back, L. E., and C. S. Bretherton, 2006: Geographic variability in the export of moist static energy and vertical motion profiles in the tropical Pacific. *Geophys. Res. Lett.,* **33,** L17810, doi:10.1029/2006GL026672.

Benedict, J. J., and D. A. Randall, 2007: Observed characteristics of the MJO relative to maximum rainfall. *J. Atmos. Sci.,* **64,** 2332–2354, doi:10.1175/JAS3968.1.

——, and ——, 2009: Structure of the Madden–Julian oscillation in the superparameterized CAM. *J. Atmos. Sci.,* **66,** 3277–3296, doi:10.1175/2009JAS3030.1.

——, E. D. Maloney, A. H. Sobel, D. M. Frierson, and L. J. Donner, 2013: Tropical intraseasonal variability in version 3 of the GFDL Atmosphere Model. *J. Climate,* **26,** 426–449, doi:10.1175/JCLI-D-12-00103.1.

Berrisford, P., D. Dee, K. Fielding, M. Fuentes, P. Kållberg, S. Kobayashi, and S. Uppala, 2009: The ERA-Interim archive, version 1.0. ECMWF Tech. Rep., 16 pp. [Available online at http://old.ecmwf.int/publications/library/ecpublications/_pdf/era/era_report_series/RS_1.pdf.]

Bladé, I., and D. L. Hartmann, 1993: Tropical intraseasonal oscillations in a simple nonlinear model. *J. Atmos. Sci.,* **50,** 2922–2939, doi:10.1175/1520-0469(1993)050<2922:TIOIAS>2.0.CO;2.

Bony, S., and K. A. Emanuel, 2005: On the role of moist processes in tropical intraseasonal variability: Cloud–radiation and moisture–convection feedbacks. *J. Atmos. Sci.,* **62,** 2770–2789, doi:10.1175/JAS3506.1.

Bretherton, C. S., and A. H. Sobel, 2002: A simple model of a convectively coupled Walker circulation using the weak temperature gradient approximation. *J. Climate,* **15,** 2907–2920, doi:10.1175/1520-0442(2002)015<2907:ASMOAC>2.0.CO;2.

——, M. E. Peters, and L. E. Back, 2004: Relationships between water vapor path and precipitation over the tropical oceans. *J. Climate,* **17,** 1517–1528, doi:10.1175/1520-0442(2004)017<1517:RBWVPA>2.0.CO;2.

——, P. N. Blossey, and M. Khairoutdinov, 2005: An energy-balance analysis of deep convective self-aggregation above uniform SST. *J. Atmos. Sci.,* **62,** 4273–4292, doi:10.1175/JAS3614.1.

Charney, J. G., 1963: A note on large-scale motions in the tropics. *J. Atmos. Sci.,* **20,** 607–609, doi:10.1175/1520-0469(1963)020<0607:ANOLSM>2.0.CO;2.

Collins, W. D., and Coauthors, 2006: The formulation and atmospheric simulation of the Community Atmosphere Model version 3 (CAM3). *J. Climate,* **19,** 2144–2161, doi:10.1175/JCLI3760.1.

Donner, L. J., C. J. Seman, R. S. Hemler, and S. M. Fan, 2001: A cumulus parameterization including mass fluxes, convective vertical velocities, and mesoscale effects: Thermodynamic and hydrological aspects in a general circulation model. *J. Climate,* **14,** 3444–3463, doi:10.1175/1520-0442(2001)014<3444:ACPIMF>2.0.CO;2.

——, and Coauthors, 2011: The dynamical core, physical parameterizations, and basic simulation characteristics of the atmospheric component AM3 of the GFDL global coupled model CM3. *J. Climate,* **24,** 3484–3519, doi:10.1175/2011JCLI3955.1.

Emanuel, K. A., 1987: An air–sea interaction model of intraseasonal oscillations in the tropics. *J. Atmos. Sci.,* **44,** 2324–2340, doi:10.1175/1520-0469(1987)044<2324:AASIMO>2.0.CO;2.

——, J. D. Neelin, and C. S. Bretherton, 1994: On large-scale circulations in convecting atmospheres. *Quart. J. Roy. Meteor. Soc.,* **120,** 1111–1143, doi:10.1002/qj.49712051902.

Frierson, D. M. W., D. Kim, I.-S. Kang, M.-I. Lee, and J. Lin, 2011: Structure of AGCM-simulated convectively coupled Kelvin waves and sensitivity to convective parameterization. *J. Atmos. Sci.,* **68,** 26–45, doi:10.1175/2010JAS3356.1.

Fuchs, Z., and D. J. Raymond, 2002: Large-scale modes of a nonrotating atmosphere with water vapor and cloud–radiation feedbacks. *J. Atmos. Sci.,* **59,** 1669–1679, doi:10.1175/1520-0469(2002)059<1669:LSMOAN>2.0.CO;2.

——, and ——, 2005: Large-scale modes in a rotating atmosphere with radiative–convective instability and WISHE. *J. Atmos. Sci.,* **62,** 4084–4094, doi:10.1175/JAS3582.1.

Haertel, P. T., G. N. Kiladis, A. Denno, and T. M. Rickenbach, 2008: Vertical-mode decompositions of 2-day waves and the Madden–Julian oscillation. *J. Atmos. Sci.,* **65,** 813–833, doi:10.1175/2007JAS2314.1.

Hannah, W. M., and E. D. Maloney, 2011: The role of moisture–convection feedbacks in simulating the Madden–Julian oscillation. *J. Climate,* **24,** 2754–2770, doi:10.1175/2011JCLI3803.1.

——, and ——, 2014: The moist static energy budget in NCAR CAM5 hindcasts during DYNAMO. *J. Adv. Model. Earth Syst.*, doi:10.1002/2013MS000272, in press.

Held, I. M., and B. J. Hoskins, 1985: Large-scale eddies and the general circulation of the troposphere. *Advances in Geophysics,* Vol. 28, Academic Press, 3–31, doi:10.1016/S0065-2687(08)60218-6.

Holloway, C. E., and J. D. Neelin, 2009: Moisture vertical structure, column water vapor, and tropical deep convection. *J. Atmos. Sci.,* **66,** 1665–1683, doi:10.1175/2008JAS2806.1.

Huffman, G. J., and Coauthors, 2007: The TRMM Multisatellite Precipitation Analysis (TMPA): Quasi-global, multiyear, combined-sensor precipitation estimates at fine scales. *J. Hydrometeor.,* **8,** 38–55, doi:10.1175/JHM560.1.

Hurrell, J. W., J. J. Hack, D. Shea, J. M. Caron, and J. Rosinski, 2008: A new sea surface temperature and sea ice boundary dataset for the Community Atmosphere Model. *J. Climate,* **21,** 5145–5153, doi:10.1175/2008JCLI2292.1.

Inness, P. M., J. M. Slingo, E. Guilyardi, and J. Cole, 2003: Simulation of the Madden–Julian oscillation in a coupled general circulation model. Part II: The role of the basic state. *J. Climate,* **16,** 365–382, doi:10.1175/1520-0442(2003)016<0365:SOTMJO>2.0.CO;2.

Khairoutdinov, M., D. Randall, and C. DeMott, 2005: Simulations of the atmospheric general circulation using a cloud-resolving model as a superparameterization of physical processes. *J. Atmos. Sci.,* **62,** 2136–2154, doi:10.1175/JAS3453.1.

——, C. DeMott, and D. Randall, 2008: Evaluation of the simulated interannual and subseasonal variability in an AMIP-style simulation using the CSU Multiscale Modeling Framework. *J. Climate,* **21,** 413–431, doi:10.1175/2007JCLI1630.1.

Kim, D., and Coauthors, 2009: Application of MJO simulation diagnostics to climate models. *J. Climate,* **22,** 6413–6436, doi:10.1175/2009JCLI3063.1.

——, A. H. Sobel, E. D. Maloney, D. M. W. Frierson, and I.-S. Kang, 2011: A systematic relationship between intraseasonal variability and mean state bias in AGCM simulations. *J. Climate,* **24,** 5506–5520, doi:10.1175/2011JCLI4177.1.

——, M.-I. Lee, D. Kim, S. Schubert, D. E. Waliser, and B. Tian, 2014a: Representation of tropical subseasonal variability of precipitation in global reanalyses. *Climate Dyn.,* **43,** 517–534, doi:10.1007/s00382-013-1890-x.

——, and Coauthors, 2014b: Process-oriented MJO simulation diagnostic: Moisture sensitivity of simulated convection. *J. Climate,* **27,** 5379–5395, doi:10.1175/JCLI-D-13-00497.1.

Kiranmayi, L., and E. D. Maloney, 2011: Intraseasonal moist static energy budget in reanalysis data. *J. Geophys. Res.,* **116,** D21117, doi:10.1029/2011JD016031.

López Carrillo, C., and D. J. Raymond, 2005: Moisture tendency equations in a tropical atmosphere. *J. Atmos. Sci.,* **62,** 1601–1613, doi:10.1175/JAS3424.1.

Madden, R. A., and P. R. Julian, 1971: Detection of a 40–50 day oscillation in the zonal wind in the tropical Pacific. *J. Atmos. Sci.,* **28,** 702–708, doi:10.1175/1520-0469(1971)028<0702:DOADOI>2.0.CO;2.

Maloney, E. D., 2009: The moist static energy budget of a composite tropical intraseasonal oscillation in a climate model. *J. Climate,* **22,** 711–729, doi:10.1175/2008JCLI2542.1.

Mapes, B. E., and J. T. Bacmeister, 2012: Diagnosis of tropical biases and the MJO from patterns in the MERRA analysis tendency fields. *J. Climate,* **25,** 6202–6214, doi:10.1175/JCLI-D-11-00424.1.

Moorthi, S., and M. J. Suarez, 1992: Relaxed Arakawa–Schubert: A parameterization of moist convection for general circulation models. *Mon. Wea. Rev.,* **120,** 978–1002, doi:10.1175/1520-0493(1992)120<0978:RASAPO>2.0.CO;2.

Neelin, J. D., and I. M. Held, 1987: Modeling tropical convergence based on the moist static energy budget. *Mon. Wea. Rev.,* **115,** 3–12, doi:10.1175/1520-0493(1987)115<0003:MTCBOT>2.0.CO;2.

——, and J.-Y. Yu, 1994: Modes of tropical variability under convective adjustment and the Madden–Julian oscillation. Part I: Analytical theory. *J. Atmos. Sci.,* **51,** 1876–1894, doi:10.1175/1520-0469(1994)051<1876:MOTVUC>2.0.CO;2.

——, and N. Zeng, 2000: A quasi-equilibrium tropical circulation model—Formulation. *J. Atmos. Sci.,* **57,** 1741–1766, doi:10.1175/1520-0469(2000)057<1741:AQETCM>2.0.CO;2.

Peters, M. E., Z. M. Kuang, and C. C. Walker, 2008: Analysis of atmospheric energy transport in ERA-40 and implications for simple models of the mean tropical circulation. *J. Climate,* **21,** 5229–5241, doi:10.1175/2008JCLI2073.1.

Pritchard, M. S., and C. S. Bretherton, 2014: Causal evidence that rotational moisture advection is critical to the superparameterized Madden–Julian oscillation. *J. Atmos. Sci.,* **71,** 800–815, doi:10.1175/JAS-D-13-0119.1.

Raymond, D. J., 2000: Thermodynamic control of tropical rainfall. *Quart. J. Roy. Meteor. Soc.,* **126,** 889–898, doi:10.1002/qj.49712656406.

——, 2014: Sources and sinks of entropy in the atmosphere. *J. Adv. Model. Earth Syst.,* doi:10.1002/2013MS000247, in press.

——, and Z. Fuchs, 2007: Convectively coupled gravity and moisture modes in a simple atmospheric model. *Tellus,* **59A,** 627–640, doi:10.1111/j.1600-0870.2007.00268.x.

——, and S. L. Sessions, 2007: Evolution of convection during tropical cyclogenesis. *Geophys. Res. Lett.,* **34,** L06811, doi:10.1029/2006GL028607.

——, and Z. Fuchs, 2009: Moisture modes and the Madden–Julian oscillation. *J. Climate,* **22,** 3031–3046, doi:10.1175/2008JCLI2739.1.

——, S. L. Sessions, and Z. Fuchs, 2007: A theory for the spinup of tropical depressions. *Quart. J. Roy. Meteor. Soc.,* **133,** 1743–1754, doi:10.1002/qj.125.

——, S. Sessions, A. Sobel, and Z. Fuchs, 2009: The mechanics of gross moist stability. *J. Adv. Model. Earth Syst.,* 1(9), doi:10.3894/JAMES.2009.1.9.

Reynolds, R. W., N. A. Rayner, T. M. Smith, D. C. Stokes, and W. Wang, 2002: An improved in situ and satellite SST analysis for climate. *J. Climate,* **15,** 1609–1625, doi:10.1175/1520-0442(2002)015<1609:AIISAS>2.0.CO;2.

Salby, M. L., and H. H. Hendon, 1994: Intraseasonal behavior of clouds, temperature, and motion in the tropics. *J. Atmos. Sci.,* **51,** 2207–2224, doi:10.1175/1520-0469(1994)051<2207:IBOCTA>2.0.CO;2.

Sessions, S. L., S. Sugaya, D. J. Raymond, and A. H. Sobel, 2010: Multiple equilibria in a cloud-resolving model using the weak temperature gradient approximation. *J. Geophys. Res.,* **115,** D12110, doi:10.1029/2009JD013376.

Sherwood, S. C., 1999: Convective precursors and predictability in the tropical western Pacific. *Mon. Wea. Rev.,* **127,** 2977–2991, doi:10.1175/1520-0493(1999)127<2977:CPAPIT>2.0.CO;2.

Sobel, A., and E. Maloney, 2012: An idealized semi-empirical framework for modeling the Madden–Julian oscillation. *J. Atmos. Sci.,* **69,** 1691–1705, doi:10.1175/JAS-D-11-0118.1.

——, and ——, 2013: Moisture modes and the eastward propagation of the MJO. *J. Atmos. Sci.,* **70,** 187–192, doi:10.1175/JAS-D-12-0189.1.

——, J. Nilsson, and L. M. Polvani, 2001: The weak temperature gradient approximation and balanced tropical moisture waves. *J. Atmos. Sci.,* **58,** 3650–3665, doi:10.1175/1520-0469(2001)058<3650:TWTGAA>2.0.CO;2.

——, G. Bellon, and J. Bacmeister, 2007: Multiple equilibria in a single-column model of the tropical atmosphere. *Geophys. Res. Lett.,* **34,** L22804, doi:10.1029/2007GL031320.

——, E. D. Maloney, G. Bellon, and D. M. Frierson, 2010: Surface fluxes and tropical intraseasonal variability: A reassessment. *J. Adv. Model. Earth Syst.,* **2**(2), doi:10.3894/JAMES.2010.2.2.

Su, H., and J. D. Neelin, 2002: Teleconnection mechanisms for tropical Pacific descent anomalies during El Niño. *J. Atmos. Sci.,* **59,** 2694–2712, doi:10.1175/1520-0469(2002)059<2694:TMFTPD>2.0.CO;2.

Sugiyama, M., 2009: The moisture mode in the quasi-equilibrium tropical circulation model. Part I: Analysis based on the weak temperature gradient approximation. *J. Atmos. Sci.,* **66,** 1507–1523, doi:10.1175/2008JAS2690.1.

Tokioka, T., K. Yamazaki, A. Kitoh, and T. Ose, 1988: The equatorial 30–60 day oscillation and the Arakawa–Schubert penetrative cumulus parameterization. *J. Meteor. Soc. Japan,* **66,** 883–901.

Waliser, D., and Coauthors, 2009: MJO simulation diagnostics. *J. Climate,* **22,** 3006–3030, doi:10.1175/2008JCLI2731.1.

Wang, B., 1988: Dynamics of tropical low-frequency waves: An analysis of the moist Kelvin wave. *J. Atmos. Sci.,* **45,** 2051–2065, doi:10.1175/1520-0469(1988)045<2051:DOTLFW>2.0.CO;2.

——, and H. Rui, 1990: Dynamics of the coupled moist Kelvin–Rossby wave on an equatorial β-plane. *J. Atmos. Sci.,* **47,** 397–413, doi:10.1175/1520-0469(1990)047<0397:DOTCMK>2.0.CO;2.

Wang, S., and A. H. Sobel, 2011: Response of convection to relative sea surface temperature: Cloud-resolving simulations in two and three dimensions. *J. Geophys. Res.,* **116,** D11119, doi:10.1029/2010JD015347.

——, and ——, 2012: Impact of imposed drying on deep convection in a cloud-resolving model. *J. Geophys. Res.,* **117,** D02112, doi:10.1029/2011JD016847.

Wheeler, M., and G. N. Kiladis, 1999: Convectively coupled equatorial waves: Analysis of clouds and temperature in the wavenumber–frequency domain. *J. Atmos. Sci.,* **56,** 374–399, doi:10.1175/1520-0469(1999)056<0374:CCEWAO>2.0.CO;2.

Yu, L. S., and R. A. Weller, 2007: Objectively analyzed air–sea heat fluxes for the global ice-free oceans (1981–2005). *Bull. Amer. Meteor. Soc.,* **88,** 527–539, doi:10.1175/BAMS-88-4-527.

Zhang, C., 2005: Madden–Julian Oscillation. *Rev. Geophys.,* **43,** RG2003, doi:10.1029/2004RG000158.

——, M. Dong, S. Gualdi, H. H. Hendon, E. D. Maloney, A. Marshall, K. R. Sperber, and W. Wang, 2006: Simulations of the Madden–Julian oscillation in four pairs of coupled and uncoupled global models. *Climate Dyn.,* **27,** 573–592, doi:10.1007/s00382-006-0148-2.

Zhang, G. J., 2002: Convective quasi-equilibrium in midlatitude continental environment and its effect on convective parameterization. *J. Geophys. Res.,* **107,** 4220, doi:10.1029/2001JD001005.

——, and N. A. McFarlane, 1995: Sensitivity of climate simulations to the parameterization of cumulus convection in the Canadian climate center general circulation model. *Atmos.–Ocean,* **33,** 407–446, doi:10.1080/07055900.1995.9649539.